Aerodynamic Shape Optimization of a Box-Wing Regional Aircraft Based on the Reynolds-Averaged Navier-Stokes Equations

Timothy Chau* and David W. Zingg†

Institute for Aerospace Studies, University of Toronto

4925 Dufferin St., Toronto, Ontario, M3H 5T6, Canada

The box wing is an unconventional aircraft configuration that has the potential to provide dramatic savings in fuel consumption relative to the conventional cantilever wing. In order to further develop and evaluate this potential, aerodynamic shape optimization based on the Reynolds-averaged Navier-Stokes equations is applied to the aerodynamic design of a box-wing and cantilever-wing regional aircraft, with the latter serving as a performance baseline. The design of each aircraft is based on the 1,850 nmi range Embraer E190 regional jet, and a nominal cruise mission is considered in which 100 passengers are to be transported 500 nmi at a Mach number of 0.78 and an altitude of 36,000 ft. Results indicate that an optimized box-wing regional aircraft with a height-to-span ratio of 0.25 burns 7.2% less fuel than a similarly optimized conventional baseline of the same span and lift. The optimizer was found to favor increasing both height-to-span ratio and stagger-to-span ratio to reduce induced drag, despite the incurrence of added wetted area from the vertical tip fins. Fore and aft wing sweep angles reached their maximum and minimum bounds, respectively, and the optimized box wing was found to have a 46:54 load distribution between the two lifting surfaces. The chord-lengths of the vertical tip fins were minimized, indicating that only a small side-force distribution is required to complete the minimum induced drag closed-loop circulation pattern.

Nomenclature

η	Spanwise location (or equivalent)
θ	Twist design variable
$\mathcal{C}_{\text{geo}}$	Vector of geometric equality constraints
$\mathcal{G}_{\text{geo}}$	Vector of geometric inequality constraints
a	Speed of sound
b	Span
C_D	Drag coefficient
$C_{D_{\text{W}}}$	Drag coefficient of the wing (or wing and tail)
$C_{D_{\text{F}}}$	Drag coefficient of the fuselage
$C_{D_{\text{V}}}$	Drag coefficient of the vertical stabilizer
C_L	Lift coefficient
C_M	Pitching moment coefficient
C_p	Pressure coefficient
c_{xz}	Taper design variable
c_{z_i}	Section shape design variable
c_T	Thrust specific fuel consumption
D	Drag

*Ph.D. Candidate, AIAA Student member, tim.chau@mail.utoronto.ca

†Professor, University of Toronto Distinguished Professor of Computational Aerodynamics and Sustainable Aviation, Associate Fellow AIAA, dwz@oddjob.utias.utoronto.ca

e	Span efficiency
h/b	Height-to-span ratio
L	Lift
L/D	Lift-to-drag ratio
L/D_{W}	Lift-to-drag ratio of the wing (or wing and tail)
l/b	Stagger-to-span ratio
M	Mach number
R	Range
S	Planform area
S_{wet}	Wetted area
V	Volume
$\mathbf{v}$	Vector of design variables
W	Weight
x,y,z	Cartesian coordinates
x_{CG}, z_{CG}	Center of gravity coordinates
x_V, z_V	Volume centroid coordinates
x_{AC}, z_{AC}	Aircraft body center of gravity coordinates
y^+	Nondimensional off-wall distance

Acronyms

AR	Aspect Ratio
CG	Center of Gravity
FFD	Free-Form Deformation
MAC	Mean Aerodynamic Chord
MTOW	Maximum Takeoff Weight
OEW	Operating Empty Weight
RANS	Reynolds-Averaged Navier-Stokes
SAT	Simultaneous Approximation Term
SBP	Summation-By-Parts
SNOPT	Sparse Nonlinear OPTimizer

I. Introduction

Today, the rate at which the demand for air travel is increasing is far exceeding that at which annual improvements to fuel efficiency are being realized. As such, game-changing advances in aircraft technology must be attained if the future of commercial aviation is to remain environmentally sustainable. One solution is to explore unconventional aircraft configurations that have the potential to provide major savings in fuel burn relative to the ubiquitous conventional cantilever wing.

The box-wing aircraft configuration is one such design. The box wing consists of a back-swept fore wing and a forward-swept aft wing interconnected at the wing tips by a pair of vertical fins. The fore and aft wings are of equal span and are characterized by minimal or zero dihedral, with the fore wing often positioned at the bottom of the fuselage, and the aft wing typically attached to the top of the vertical stabilizer. In this way, the box wing resembles a rectangle, or "box" when viewed from the front. As a nonplanar and closed wing system, the box wing experiences less induced drag compared to a planar wing of the same span and lift. This comes from the distribution of circulation over a greater mass of air, which leads to a reduction in average kinetic energy added to the flow,[1] and from having more gradual circulation gradients, especially near the wing tips.[2]

In 1924, Prandtl called the box wing the "best wing system" and described it as being superior to all other wing configurations for a given span, height, and lift.[3] This conclusion was based on classical lifting-line theory, which was first used to demonstrate that a biplane experiences less induced drag when compared to an optimum monoplane with the same span and lift. The benefit was shown to improve when moving from a biplane to a triplane, and it was argued that this trend would continue with the further addition

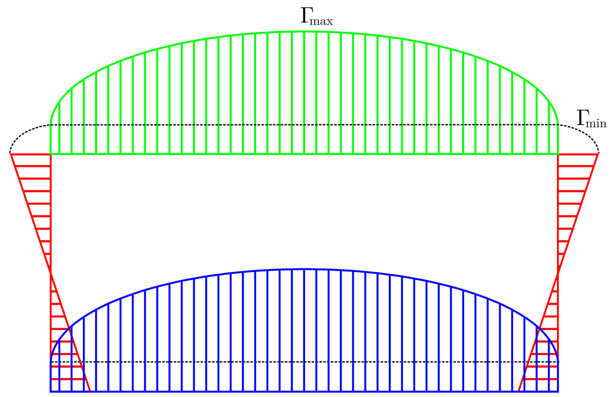

Figure 1: Circulation of a box wing based on linear aerodynamic theory, with the lift distribution over the fore and aft wings shown in blue and green, respectively, and the side-force distribution over the vertical tip fins shown in red.

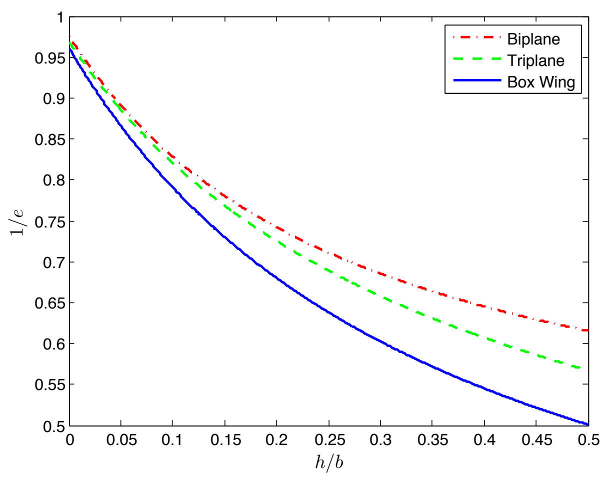

Figure 2: Relationship between induced drag and height-to-span ratio based on linear aerodynamic theory, relative to an optimum monoplane.

of lifting surfaces. In the limit of a multiplane with an infinite number of lifting surfaces, assuming the lift could be maintained, the lift distribution was found to reflect that of a box-wing configuration, namely, a closed loop circulation composed of a constant plus an elliptical distribution on the fore and aft wings, and a butterfly-shaped distribution on the vertical tip fins, as shown in Figure 1.

In the same paper, Prandtl presented an equation for the induced drag experienced by a box wing, relative to that of an optimum monoplane with the same span and lift, given by,

$$\frac{1}{e} \approx \frac{1 + 0.45(h/b)}{1.04 + 2.81(h/b)}, \tag{1}$$

where e is the span efficiency of the box wing, and h/b is the height-to-span ratio. Here, the span efficiency of the optimum monoplane was taken to be unity, based on an elliptical lift distribution. Meanwhile, the nonplanar nature of the box wing allows for span efficiencies greater than one. This relationship is shown in Figure 2; for comparison, the relative performance of a biplane and a triplane are also shown, which illustrates that the induced drag decreases as the number of lifting surfaces tends to infinity.

Equation (1) indicates that for a height-to-span ratio of 0.3, the box wing experiences only 60% of the induced drag experienced by an optimum monoplane. Since induced drag constitutes about 40% of the total drag of a typical commercial aircraft,[1] this translates to an overall drag reduction of 16%. According to Munk's stagger theorem,[4] these trends apply to box wings that are swept, as long as the lift distribution remains the same, making the box wing an attractive option for transonic aircraft.

The box-wing configuration is also robust in that it maintains its aerodynamic efficiency at off-design conditions. Such an advantage comes from being a closed wing system, which allows a constant vortex loop to be added to the circulation with minimal penalty to induced drag.[1] Indeed, this property was corroborated by Demasi et al.,[5] who found the optimum partitioning of total lift between the fore and aft wings, originally assumed to be equal by Prandtl,[3] to be nonunique. Specifically, Demasi et al. demonstrated through a vortex panel method that the optimum distribution of total lift could be shifted by a constant from one wing to the other, while maintaining the same span efficiency.

Furthermore, the box-wing configuration is attractive for reasons of safety. In particular, the box wing has exceptional longitudinal stability and control characteristics owing to its ability to provide "pure pitch," through equally effective control surfaces on the fore and aft wings.[6] The box wing also has favorable characteristics for stall recovery. This stems from the tendency of the fore wing to stall before the aft wing.[7] In such an event, the downwash on the aft wing is alleviated, allowing it to produce a large pitch-down moment to restore the state of the aircraft.

In 1972, Lockheed recognized the potential advantages of the box-wing configuration and initiated preliminary investigations for applications in commercial aviation. The first of these was done by Miranda,[8] who recovered the aerodynamic trends predicted by Prandtl, through low speed wind tunnel tests. Subsequently, Lange et al.[9] performed a feasibility study on a long range, Mach 0.95 box-wing aircraft with a height-to-span ratio of 0.3. A number of unique design features were considered, such as a forward-swept vertical stabilizer for accommodating a forward-shifted wing system centered about the pitch axis, and a "gull-like" aft wing, which provided a compromise between span efficiency and increased ramp weight. However, the box wing was found to experience symmetric and antisymmetric instabilities well below the target flutter speed. In addition, it was found that for a design with minimum maximum takeoff weight (MTOW), gains in aerodynamic performance were marginal, and no reduction in ramp weight could be achieved relative to a similarly-sized cantilever wing. As a result, it was concluded that the box wing might only be effective at lower Mach numbers, where structural requirements are less stringent, and flutter is less of a concern.

In 1986, Wolkovitch,[10] a pioneer of the joined-wing aircraft configuration, commented on the work done by Lange et al, asserting that the poor aerodynamic performance of the box wing was likely a result of using conventional airfoil profiles in its design. In particular, Wolkovitch suggested that the aerodynamic advantages of the box wing, similar to the joined wing, can only be realized if the airfoils are tailored towards the unique flow conditions experienced by the neighboring wings. Such an assessment agrees with the findings of Addoms and Spaid,[7] who determined that the camber of the airfoils used in the design of biplanes must substantially differ from those used by monoplanes as a consequence of the induced flow curvature. However, Wolkovitch conceded that the success of the box wing would ultimately hinge on a viable solution to the flutter problem.

More recently, interest in the box-wing configuration has been renewed, primarily to the credit of Frediani,[6] who has been active in the development of what he calls the "PrandtlPlane." For addressing aeroelastic instabilities, Frediani sought to increase the structural stiffness of the wing system, while ensuring that any penalty to structural weight was kept to a minimum. To this end, he proposed a tail configuration with twin vertical stabilizers, maximally distanced apart. This feature was included in a structural analysis done by Canto et al.,[11] who demonstrated that a feasible box wing could be designed using aluminum structures with the same wing weight to MTOW ratio as a conventional cantilever wing. Other mitigation measures included placing more priority on structural reinforcements against out-of-plane bending moments (as also recommended by Wolkovitch[10] for the joined-wing configuration), and increasing the fore wing skin thickness.[12] Frediani went on to consider applications in commercial aviation[13,14] and for personal use,[15] with each aircraft designed for lower Mach numbers, as recommended by Lange et al.[9] These studies, as well as many other research efforts focused on the box-wing aircraft configuration, are included in an extensive review by Cavallaro and Demasi.[22]

Now, the work of Frediani and others suggest that the concerns surrounding the box-wing configuration with regard to flutter and structural weight may not be as insurmountable as initially thought. However, further research is still required to determine whether there exists a viable solution. In the meantime, the aerodynamic performance of the box-wing configuration must also be studied in more detail. Indeed, many of the proclaimed advantages of the box wing were founded on linear aerodynamic theory; for more realistic flow conditions, however, nonlinear aerodynamics must be explored. Given that the primary advantages of the box-wing configuration are aerodynamic in nature, nonlinear aerodynamics will be a key driver in deciding its future as a next generation aircraft.

Today, numerical methods in aerodynamic shape optimization have enabled in-depth studies of the box-wing configuration. One such study was done by Andrews and Perez,[16] who used low-fidelity aerodynamic shape optimization to perform a parametric study of a box-wing regional jet. Key geometric parameters were considered such as height-to-span ratio, stagger-to-span ratio, and the relative planform area between the fore and aft wings. At each design point, a drag minimization problem was solved with respect to twist and taper design variables, subject to lift, trim, static margin, and stall constraints. From this, several fundamental trends and trade-offs were observed.

For one, induced drag was found to be inversely proportional to both the height-to-span ratio and the stagger-to-span ratio, with each parameter exhibiting diminishing returns at higher values; such an outcome should come as no surprise given that there exists a design point for which the viscous drag from the increase in wetted area eclipses the savings in induced drag. Meanwhile, the relative planform area was found to have the least effect on aerodynamic performance, whereas the trim and static margin constraints produced only a small penalty in total drag, as asserted by Kroo.[1]

Following this work, Andrews and Perez[17] applied low-fidelity multidisciplinary optimization to the design of a box-wing aircraft based on the Bombardier CRJ-200. A cruise Mach number of 0.74 was considered at an altitude of 37,000 ft, and the optimization accounted for the complete mission profile. The framework included aerodynamics, structures, and propulsion, thus allowing for interdisciplinary trade-offs. The result of the optimization was a 6% reduction in fuel burn over a similarly-sized conventional aircraft, hence demonstrating the potential savings offered by regional class box-wing jetliners.

The advantage of low-fidelity optimization is that it can provide the designer with a better understanding of the design space by identifying trends and trade-offs at a relatively low computational cost. However, these linear aerodynamic models are not capable of accurately resolving critical adverse effects such as shock waves and boundary-layer separation, if at all. Nonlinear interference effects that characterize box wing flow fields are also beyond the regime of low-fidelity methods. A deeper understanding of the design and performance potential of a box-wing regional aircraft will therefore require methods of higher fidelity. Although much more expensive in terms of computational cost, high-fidelity aerodynamic shape optimization tools provide a physics-based approach to design that has the ability to identify and eliminate these adverse flow features.

In recent studies done by Gagnon and Zingg,[18,19] wave drag and nonlinear interference effects were accounted for through the application of aerodynamic shape optimization based on the Euler equations. In particular, aerodynamic shape optimization was applied to the aerodynamic design and performance evaluation of a box-wing regional aircraft based on the Bombardier CRJ-1000. A nominal mission was considered in which 100 passengers were to be transported 500 nmi at a Mach number of 0.78 and an altitude of 36,000 ft. For the cruise segment alone, the optimized box wing was found to provide a 43% reduction in induced drag, relative to an equivalent conventional tube-and-wing. A trade study was also presented in which a total of five optimization studies were conducted, with each subject to progressively more design variables and constraints. From this, the box wing was found to have the freedom to redistribute the total lift from one wing to the other for satisfying design constraints such as trim, static margin, and root bending moment constraints, while simultaneously maintaining aerodynamic performance.

The next step needed for the aerodynamic investigation of the box wing is to include viscous effects through aerodynamic shape optimization based on the Reynolds-averaged Navier-Stokes (RANS) equations. RANS-based aerodynamic shape optimization enables trade-offs between induced drag and viscous drag, and is necessary to ensure fully attached boundary layers.[20,21] The simulation of viscous effects, in addition, allows the optimizer to account for the shorter chord lengths of the box-wing configuration, which may cause it to experience higher viscous drag compared to an equivalent conventional cantilever wing.

The objective of the present study is therefore to further understand the aerodynamic design and performance potential of the box-wing configuration for regional-class aircraft through the application aerodynamic shape optimization based on the RANS equations. RANS-based aerodynamic shape optimization is applied to the aerodynamic design of a box-wing and cantilever-wing regional aircraft, with the latter serving as a performance baseline. For the box wing, a preliminary exploratory optimization is performed to investigate aerodynamic trends and trade-offs, and to refine the initial geometry for a subsequent lift-constrained drag minimization with reduced geometric freedom.

The paper is organized as follows. Section II provides a brief overview of the aerodynamic shape optimization framework based on the RANS equations. Section III describes the problem setup for each aerodynamic shape optimization problem and includes details on aircraft size, mission, and design, as well as initial geometry, computational mesh, and geometry control. Sections IV, V, and VI present the results for the lift-constrained drag minimization of the cantilever wing, the exploratory optimization of the box wing, and the lift-constrained drag minimization of the box wing, respectively. A weight sensitivity study is provided in Section VII, and conclusions are drawn in Section VIII.

II. Aerodynamic Shape Optimization Methodology

The aerodynamic design and performance evaluations of the box-wing and cantilever-wing configurations are performed using a high-fidelity aerodynamic shape optimization framework. It comprises (1) an integrated geometry parameterization and mesh-movement scheme based on linear elasticity,[23] (2) a free-form and axial deformation geometry control system,[24] (3) a Newton-Krylov-Schur flow solver for the RANs equations fully coupled with the one-equation Spalart-Allmaras turbulence model,[25] (4) the discrete-adjoint method[26–28] for gradient evaluation, and (5) SNOPT[29] for gradient-based optimization. In what follows, a brief discussion of each component is provided.

The integrated geometry parameterization and mesh-movement scheme provides a fast and efficient means for updating the mesh following a deformation to the aerodynamic surfaces. For this strategy, each block of the computational domain is parameterized with a B-spline volume, with an equal number of grid nodes contained within each knot interval. This results in a lattice of volume control points which mimic the spatial distribution of the grid nodes. The mesh-movement scheme can then be applied to the coarse mesh of volume control points rather than the mesh nodes themselves, without loss of generality. This leads to a significant reduction in computational cost, since the number of volume control points is typically fewer than the number of grid nodes by two to three orders of magnitude. Once the subset of volume control points that lie on the boundaries of the aerodynamic surfaces are perturbed, changes are propagated throughout the control grid through a robust mesh-movement scheme based on a linear elasticity model.[23] The updated mesh can then be regenerated analytically.

Geometry control is provided by the free-form and axial deformation method,[24] which is an attractive option for its ability to provide rapid and smooth deformations, and for its mathematical intuitiveness. This method employs free-form deformation (FFD) volumes, defined as B-spline volume lattices, that transform an embedded object of interest as the FFD-volumes themselves are deformed. In this way, the shape deformation process is dissociated from the shape representation of the embedded object, which allows for the use of fewer yet more intuitive design variables. As with Gagnon and Zingg,[24] the B-spline control points are embedded within the FFD volumes, as opposed to the surface mesh nodes. This ensures that the analytical representation of the underlying surface is retained. The FFD volumes comprise a number of FFD-volume cross-sections which consist of an equal number of FFD control points on either side of a given aerodynamic surface. These FFD-volume cross-sections provide local shape control through twist, taper, and section shape design variables. Attached to the leading edge of each FFD volume is an axial curve which coincides with the local origin of each FFD-volume cross-section. These axial curves are defined as B-splines and provide translational degrees of freedom.

In order to compute aerodynamic functionals, a three-dimensional structured multi-block flow solver is used. The algorithm is an implicit parallel Newton-Krylov-Schur flow solver that is used to solve the RANS equations fully coupled with the one-equation Spalart-Allmaras turbulence model.[30] The RANS equations are discretized through second-order centered difference summation-by-parts (SBP) operators,[31] and simultaneous-approximation terms (SATs) are used to enforce boundary conditions and interblock coupling weakly. Together, SBP-SAT operators provide excellent numerical stability properties and efficient parallel performance, while only requiring C^0 mesh continuity at block interfaces.[32] To aid in stabilizing the solution around shocks, a pressure sensor is used to control the activation of artificial dissipation. This work uses 2nd- and 4th-difference scalar dissipation operators,[33,34] but matrix dissipation is also available.[35] Boundary layers are assumed to be fully turbulent.

Numerical optimization is performed with the software package SNOPT,[29] a gradient-based optimization algorithm that uses sequential quadratic programming. SNOPT is capable of solving large-scale nonlinear problems subject to both linear and nonlinear constraints, and hence is well-suited for high-fidelity aerodynamic shape optimization where hundreds of design variables are often involved. For the evaluation of the objective function gradient, as well as constraint gradients that depend on the flow solution, the discrete-adjoint method is employed,[26–28] which is virtually independent of the number of design variables involved. For geometric constraints, gradients are calculated either analytically or through the complex-step method.[36]

SNOPT provides a number of metrics for tracking convergence. Of particular interest are Feasibility, Merit, and Optimality. Feasibility represents how well the nonlinear constraints are satisfied, while Merit represents a combination of Feasibility and the objective function, and corresponds to the latter when Feasibility is negligible, i.e. when the nonlinear constraints are satisfied. Optimality represents the gradient of the augmented objective function, which is driven towards zero when approaching a local (or global) optimum. In this work, aerodynamic designs are considered optimal when the Merit function aymptotes, Feasibility has been satisfied to a tolerance of 10^{-6}, and Optimality has reduced by at least two orders of magnitude. Deep convergence of Optimality is preferred, but is often difficult to achieve for constrained optimization problems in three dimensions.

III. Problem Setup

A. Design Mission

The size and design mission of each aircraft is based on the Embraer E190 regional jet. Steady, level flight is considered at a Mach number of 0.78 and an initial cruise altitude of 36,000 ft. A nominal cruise mission is considered where each aircraft is to transport 100 passengers and 5 crew over a distance of 500 nmi, with a 100 nmi fuel reserve.

The performance of each aircraft is evaluated using the Breguet range equation (cruise/climb) given by

$$W_{\text{fuel}} = W_{\text{final}} \left[\exp\left(\frac{c_T R}{aM(L/D)} \right) - 1 \right], \tag{2}$$

where W_{final} is the final aircraft weight at the end of cruise, c_T is the thrust specific fuel consumption, R is the cruise range, a and M are the speed of sound and the Mach number at cruise, respectively, and L/D is the lift-to-drag ratio. Of particular interest is the reduction in fuel burn offered by the box-wing configuration relative to the cantilever wing. This is represented by the difference in fuel consumption between the two aircraft divided by the fuel consumed by the conventional baseline. Each aircraft is driven by a pair of CF34-10E engines that each have an assumed thrust specific fuel consumption of 0.64 lb/lbf/h and an approximate weight of 3700 lb.

B. Initial Geometry

The initial geometry of the cantilever-wing configuration consists only of the main wing and the horizontal stabilizer, while for the box-wing configuration, the initial geometry comprises only the wing system. The fuselage and engines are not modeled since the focus of the present study is on the aerodynamic advantages offered by the wing system of the box-wing configuration over the conventional cantilever wing. The carry-through regions of the wing geometries are included to compensate for the lift that a fuselage would otherwise provide. Although we would prefer to remove the carry-through regions altogether and to reduce the lift constraint by the lift carried by the fuselage, such an approach is not possible for the box-wing configuration because of the aft wing. The vertical stabilizer is also not modeled since its design is based on criteria outside of cruise.

However, in order to better represent the performance of the entire aircraft, viscous drag contributions from the fuselage and the vertical stabilizer are accounted for post-optimization. For the fuselage, the drag coefficient is based on the viscous drag of the conventional wing-body-tail geometry of Reist and Zingg[37] and has a value of $C_{D_\text{F}} = 0.0106$ with a reference area of $S = 935$ ft^2. Meanwhile, the drag coefficient of the vertical stabilizer is determined by performing an isolated RANS-based flow analysis and has a value of $C_{D_\text{V}} = 0.0011$ based on the same reference area. Here, we assume that the vertical stabilizer has a similar wetted area and therefore viscous drag as that of the conventional cantilever wing for sufficient stability and control.

The initial planforms of the cantilever-wing and box-wing aircraft configurations are shown in Figure 3. The design of the cantilever wing is based on the Embraer E190 regional jet,[38] while for the box wing, the initial planform is an extension of the cantilever wing. More specifically, the fore wing is nearly identical to the main wing of the conventional baseline, with a root chord length of 21 ft and a leading-edge sweep angle of +28 degrees. The aft wing has a root chord length equal to that of the horizontal stabilizer of the cantilever-wing configuration, i.e. 11.3 ft, with a trailing-edge sweep angle of −28 degrees to mirror the fore wing. The fore and aft wings have +2 degrees and −2 degrees of dihedral, respectively, and are

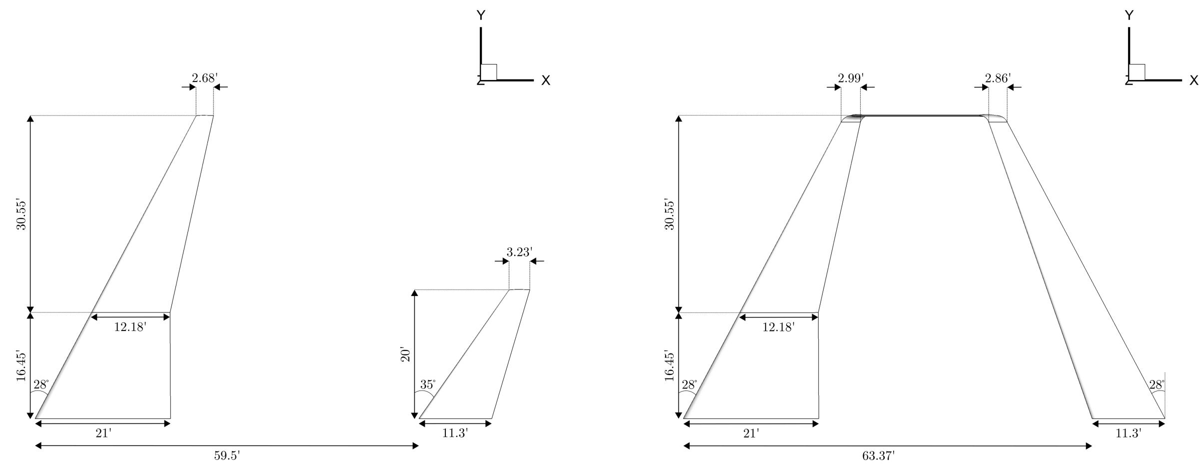

(a) Cantilever Wing

(b) Box Wing

Figure 3: Initial planforms of the cantilever-wing and box-wing aircraft configurations.

interconnected at the wing tips to the vertical tip fin by a pair of blended transitions that aid in reducing interference drag. To maximize the vertical separation of the fore and aft wings, the root of the fore wing is positioned at the bottom of the fuselage, while the root of the aft wing is stationed near the tip of the vertical stabilizer, in reference to the Embraer E190. The vertical tip fin has a constant chord length of 2.68 ft.

The cantilever wing and the box wing are of equal span at 94 ft. The initial wing-tail and wing geometries of each respective aircraft have zero twist and angle of attack, and NACA SC(2)-0012 supercritical symmetric airfoils. This provides a clean slate design that allows equally effective section shape deformations in either direction, while also presenting a reasonable starting point for transonic flow conditions.

C. Weight and Balance

For the cantilever-wing aircraft, the weight and balance calculations are done using methods based on the models of Torenbeek,[39] Kroo,[40] and Raymer.[41] These relationships are empirical formulae, derived from conventional aircraft data, which model the weight and center of gravity (CG) of the major aircraft components, and account for the aircraft systems, structures, payload, fuel, and operational items. Though of low fidelity, these approximations are sufficient for the conceptual design stage of conventional aircraft, during which detailed information is often unavailable. For the cantilever-wing configuration, the weight and balance are determined from the main wing, the horizontal and vertical stabilizers, the fuselage, and the engines.

Meanwhile, for unconventional aircraft configurations like the box wing, the use of these methods can be misleading, given the nature of the data from which these methods are derived. At the same time, calculating a weight and CG that are representative of a competitive box-wing configuration can be difficult without the use of a structural model. One alternative is to introduce low-fidelity structural approximations for modifying the empirical relationships. However, such a crude approach can detract from the relationship between aerodynamic performance and fuel burn. Instead, we assume that the weight of the box-wing configuration is equal to that of the conventional baseline. This is seen as a reasonable choice given that recent efforts[11,17] suggest that the weight of a box-wing aircraft (and in particular, the weight of its wing system) is comparable to that of a similarly-sized conventional design. In addition, setting the lift target equal to that of the cantilever-wing configuration enables a direct comparison of aerodynamic performance, given that each aircraft has the same span.

With regard to the CG of the box-wing configuration, the x-coordinate is determined by the volume centroid of the wing system, which can vary throughout the optimization process. In this way, the CG is tied to the weight distribution of the wing structure and stored fuel, both of which are assumed to be proportional to the volume of the wing system. Since the trim constraint is only dependent on the positioning

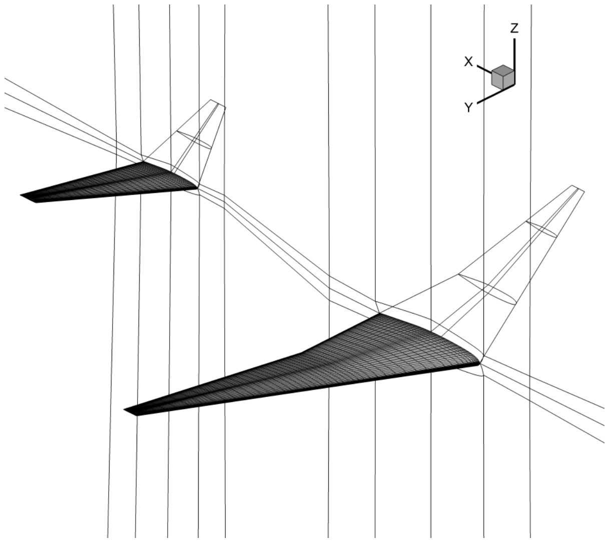

(a) Cantilever Wing

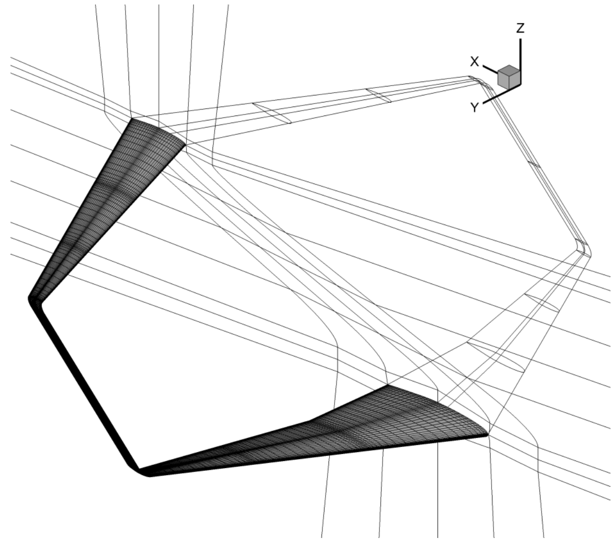

(b) Box Wing

Figure 4: Surface meshes and blocking topologies of the cantilever-wing and box-wing aircraft configurations.

of the CG relative to the fore and aft wings, contributions from the other major aircraft components are not included (i.e. the vertical stabilizer, the fuselage, and the engines). Meanwhile, the z-coordinate is determined by a weighted average between the volume centroid of the wing system, and the CG of the remaining aircraft components. Here, we assume that the ratio between the wing weight and the MTOW is 12% in accordance with typical values exhibited by conventional aircraft (again, assuming that the wing weight of the box-wing configuration is similar to that of the cantilever-wing configuration).

D. Computational Mesh

The computational domain of each aircraft is discretized through an H-topology multi-block structured grid as shown in Figure 4. For the cantilever-wing configuration, the optimization grid is partitioned across 168 blocks and consists of 2.78 million grid nodes, whereas for the box-wing configuration, the optimization grid is subdivided into 288 blocks and is made up of 5.06 million grid nodes. The performance of each aircraft is evaluated based on estimated grid converged aerodynamic functionals, which are obtained through Richardson extrapolation assuming second-order convergence. This is done with the addition of two finer grids: L1 and L2, with two and four times as many grid nodes as the optimization grid, L0, respectively.

Since the wing area is allowed to vary, it is important that we accurately capture the relevant physics throughout the optimization process. In particular, we are interested in the ratio between friction and pressure drag, and hence size the optimization grid such that this ratio is as close to the grid converged value as possible. An overview of the grids is provided in Table 1. The off-wall spacings in wall units, y^+, are based on the flow solutions of the optimized geometries.

E. Geometry Control System

As described in Section II, the aerodynamic surfaces of each aircraft are parameterized with B-splines, and the surface control points are embedded within a number of FFD volumes that drive the shape deformation process. These FFD volumes are linear in the vertical direction, and cubic in both the chordwise and the spanwise directions to ensure C^2 continuity. For the cantilever wing, the surface control points are embedded within three FFD volumes: two for the main wing and one for the horizontal stabilizer. The FFD volumes surrounding the main wing consist of 10 FFD-volume cross-sections in total, whereas the FFD volume that embeds the horizontal stabilizer consists of 5 FFD-volume cross-sections.

Meanwhile, the surface control points of the box wing are embedded within six FFD volumes: two for the fore wing, one for the aft wing, one for the vertical tip fin, and one for each blended transition. The FFD volumes surrounding the fore wing, the aft wing, and the vertical tip fin each consist of 10 FFD-volume

Table 1: Grid information.

Grid	Number of Nodes	Average Off-Wall Spacing	Average y^+
		Cantilever Wing	
L0	$2.78{\times}10^6$	$1.17{\times}10^{-6}$	0.90
L1	$5.38{\times}10^6$	$8.86{\times}10^{-7}$	0.64
L2	$10.78{\times}10^6$	$6.78{\times}10^{-7}$	0.47
		Box Wing	
L0	$5.06{\times}10^6$	$1.16{\times}10^{-6}$	0.58
L1	$9.81{\times}10^6$	$8.72{\times}10^{-7}$	0.41
L2	$19.63{\times}10^6$	$6.68{\times}10^{-7}$	0.30

Optimization is performed on L0, while L1 and L2 are used in second-order Richardson extrapolation for computing aerodynamic functionals. Average off-wall spacings are in units of mean aerodynamic chord.

cross-sections, whereas both of the FFD volumes embedding the blended transitions consist of 5 FFD-volume cross-sections each; this makes for a total of 36 unique FFD-volume cross-sections when accounting for overlaps. Each FFD-volume cross-section consists of 20 FFD control points, with 10 on either side of a given aerodynamic surface.

The FFD volumes provide twist, taper, and section shape degrees of freedom, which are realized through rotation and scaling operators. In particular, for a given FFD-volume cross-section, the degrees of freedom are defined as follows.

- **twist**: a rotation of the FFD-volume cross-section in the local xz-plane about the local origin.
- **taper**: a uniform scaling in the local xz-plane from the local origin along the local x- and z-axes.
- **section shape**: a nonuniform scaling in the local xz-plane along the local z-axis for a given control point.

These transformation operators are applied to the initial xyz-coordinates of the FFD-volume lattice at each update, with changes following a cubic interpolation between each FFD-volume cross-section. To be clear, the design variables of each FFD-volume cross-section are independent from one another, unless otherwise subject to a geometric constraint. The free-form deformation design variables are illustrated in Figure 5.

For the cantilever wing, linear axial curves are positioned at the leading edge of the main wing and the horizontal stabilizer, whereas for the box wing, linear axial curves are positioned at the leading edge of the fore and aft wings, and the vertical tip fin, while cubic axial curves are attached to the leading-edges of the two blended transitions. These axial curves define the axes of rotation for the twist design variables and consist of 5 and 11 axial curve control points in total for the cantilever-wing and box-wing configurations, respectively.

Through translation operators, these axial curve control points provide sweep, span, and dihedral degrees of freedom. More formally, the degrees of freedom for a given axial curve control point are defined as follows.

- **sweep**: a change in the x-coordinate of an axial curve control point.
- **span**: a change in the y-coordinate of an axial curve control point.
- **dihedral**: a change in the z-coordinate of an axial curve control point.

To obtain the perturbed xyz-coordinates of the axial curve control points, the design variables are added to the corresponding initial xyz-coordinates at each update. As the axial curves are deformed, the local

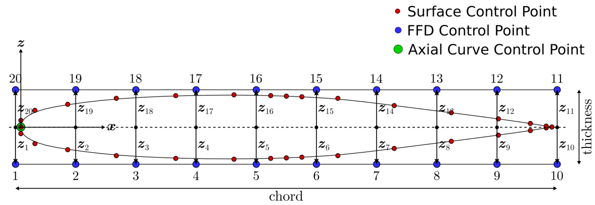

(a) Initial

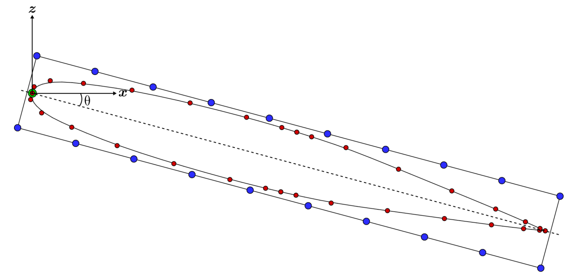

(b) Twist

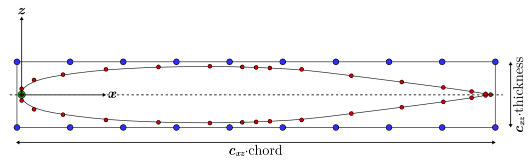

(c) Taper

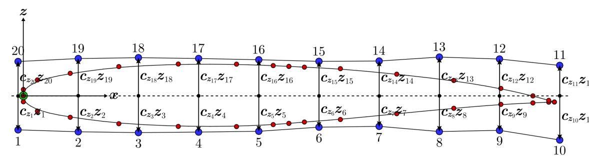

(d) Section shape

Figure 5: Free-form deformation design variables for an airfoil. The design variables are θ, c_{xz}, and c_{z_i} for twist, taper, and section shape (for a given control point, i), respectively.

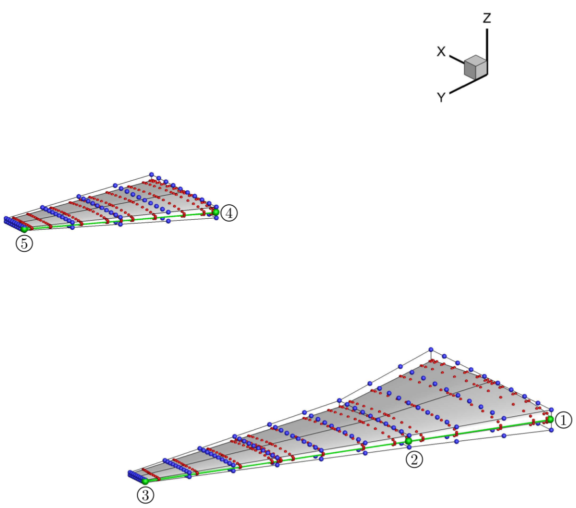

(a) Cantilever Wing

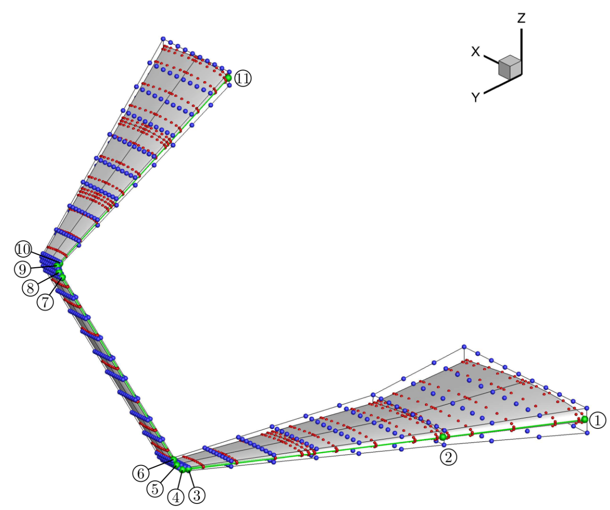

(b) Box Wing

Figure 6: Free-form and axial deformation geometry control system for aerodynamic shape optimization which comprises surface control points (red spheres), FFD volumes (black lines), FFD control points (blue spheres), axial curves (green lines), and axial curve control points (green spheres) [numbered].

coordinate systems of the FFD-volume cross-sections translate with the axial curves, as one would expect. Once again, it should be made clear that the design variables of each axial curve control point are distinct unless otherwise subject to a geometric constraint. The free-form and axial deformation geometry control system of each aircraft is shown in Figure 6. In what follows, the design variables that are active in each study will be described on a case-by-case basis.

Table 2: CTW100: Design variables and geometric constraints.

Parameter	Lower Bound	Upper Bound
	Design Variables (215)	
Angle of attack (1)	$-8°$	$+8°$
Twist (14)	$-10°$	$+10°$
Section shape (200)	50%	150%
	Geometric Constraints (104)	
Wing volume (1)	$1.25V_{\text{fuel}}$	$+\infty$
Thickness-to-chord ratio (100)	80%	$+\infty$
Linear twist (2)	–	–
Twist linking (1)	–	–

Bounds given as deviations and percentages are with respect to the initial geometry.

IV. Lift-Constrained Drag Minimization of the Cantilever Wing

Aerodynamic shape optimization based on the RANS equations is applied to the aerodynamic design of a cantilever-wing regional aircraft, herein designated as the CTW100, which stands for the 100 passenger conventional tube-and-wing aircraft. This design serves as a performance baseline for comparison with the box-wing regional aircraft. The optimization problem is to minimize drag subject to lift and trim constraints, as defined by the design mission.

A. Design Variables and Geometric Constraints

The aerodynamic shape optimization of the CTW100 involves 215 design variables: the angle of attack, 14 twist design variables (one for each FFD-volume cross-section, except at the root of the main wing where a similar degree of freedom is provided by the angle of attack), and 200 section shape design variables (one for each FFD control point surrounding the main wing). To remain consistent with the design of the Embraer E190 regional jet, the conventional wing-tail geometry does not include planform design variables. That is to say, taper, sweep, span, and dihedral design variables are not considered. Fixing the wing area to that of the Embraer E190 also ensures that the optimized CTW100 is sufficiently sized for takeoff conditions.

In lieu of structural analysis, minimum wing volume and minimum thickness-to-chord ratio constraints are imposed, which prevent the optimizer from designing arbitrarily thin aerodynamic surfaces. In particular, the wing volume is constrained to be greater than or equal to 4500 gallons for fuel storage,[38] plus 25 percent to accommodate internal wing systems such as slats and flaps. This translates to an 80 percent utilization factor for fuel storage within the wing. Meanwhile, the thickness at any given chordwise station, defined as the distance along the local z-axis between a pair of FFD control points, is constrained to be greater than or equal to 80 percent of its initial value.

For faster convergence, the redundancy in functionality between twist and section shape design variables is reduced; this is done through a linear twist constraint across each FFD volume where the twist at each intermediate FFD-volume cross-section is subject to a linear interpolation. A twist linking constraint is also imposed on the FFD-volume cross-sections of the horizontal stabilizer to maintain a symmetric airfoil design. A summary of the design variables and geometric constraints is provided in Table 2.

Table 3: CTW100: Design summary.

PAX	b [ft]	S [ft^2]	AR [–]	MAC [ft]	OEW [lb]	MTOW [lb]	Weight* [lb]
100+5	94	997	8.9	13.1	59,200	105,500	91,400

*The weight of the aircraft at the start of the nominal cruise mission.

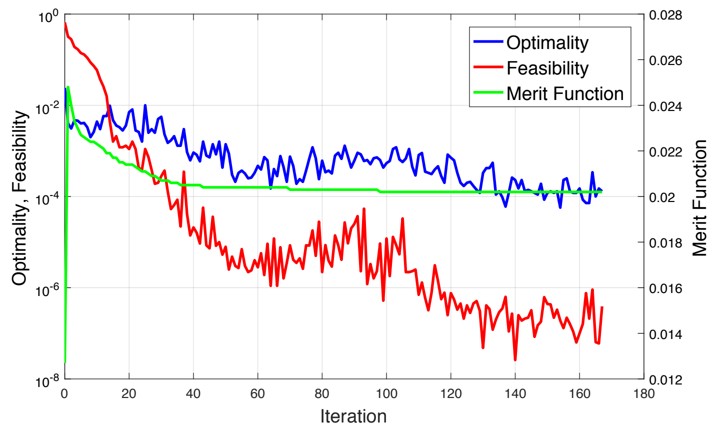

Figure 7: CTW100: Optimization history. The Merit function represents C_{D_W}.

B. Lift-Constrained Drag Minimization

The optimization problem is formulated as follows:

$$\begin{aligned} \text{minimize} \quad & C_{D_\mathrm{W}}, \\ \text{w.r.t.} \quad & \mathbf{v}, \\ \text{s.t.} \quad & L = W, \quad C_M = 0, \\ & \mathcal{C}_\mathrm{geo} = 0, \quad \mathcal{G}_\mathrm{geo} \geq 0, \end{aligned}$$

where C_{D_W} is the drag coefficient of the wing-tail geometry, $\mathbf{v} = [\alpha, \mathbf{v}_\mathrm{geo}^\mathrm{T}]^\mathrm{T}$ is the vector of design variables, and $\mathcal{C}_\mathrm{geo}$ and $\mathcal{G}_\mathrm{geo}$ are the vectors of geometric equality and inequality constraints, respectively. As provided in Table 2, $\mathcal{C}_\mathrm{geo}$ consists of the linear twist and twist linking constraints, while $\mathcal{G}_\mathrm{geo}$ includes the minimum wing volume and minimum thickness-to-chord ratio constraints. A nominal cruise mission is considered at a Mach number of 0.78 and an altitude of 36,000 ft, which corresponds to a Reynolds number of 23.6×10^6, based on a mean aerodynamic chord (MAC) of 13.1 ft. The maximum weight at cruise is 91,400 lb, as determined from the empirical weight models. A summary of the CTW100 design is provided in Table 3.

An optimized design was obtained following the completion of 167 design iterations on 168 processors. As shown in Figure 7, the end of the optimization is marked by the asymptotic behavior of the Merit function, the convergence of Feasibility to an absolute tolerance of 10^{-6}, and a reduction in Optimality by approximately two orders of magnitude. With Feasibility satisfied, the Merit function represents the drag coefficient of the wing-tail geometry, which was found to be $C_{D_\mathrm{W}} = 0.0202$ on the optimization grid. The optimized CTW100 has a wing area of $S = 997$ ft^2 and a wing-tail wetted area of $S_\mathrm{wet} = 1,320$ ft^2. The design angle of attack was found to be 6.4 degrees.

As illustrated in Figure 8, the upper and lower surfaces of the optimized CTW100 are characterized by smooth pressure gradients, indicating that wave drag has been eliminated. Figure 9(a) shows that for the optimized CTW100, the spanwise lift distribution over the main wing is close to elliptical but is shifted towards the wing root as a consequence of the trim constraint. Indeed, with the majority of the outboard region positioned aft of the CG, inboard loading was found to be favorable for counterbalancing the nose-

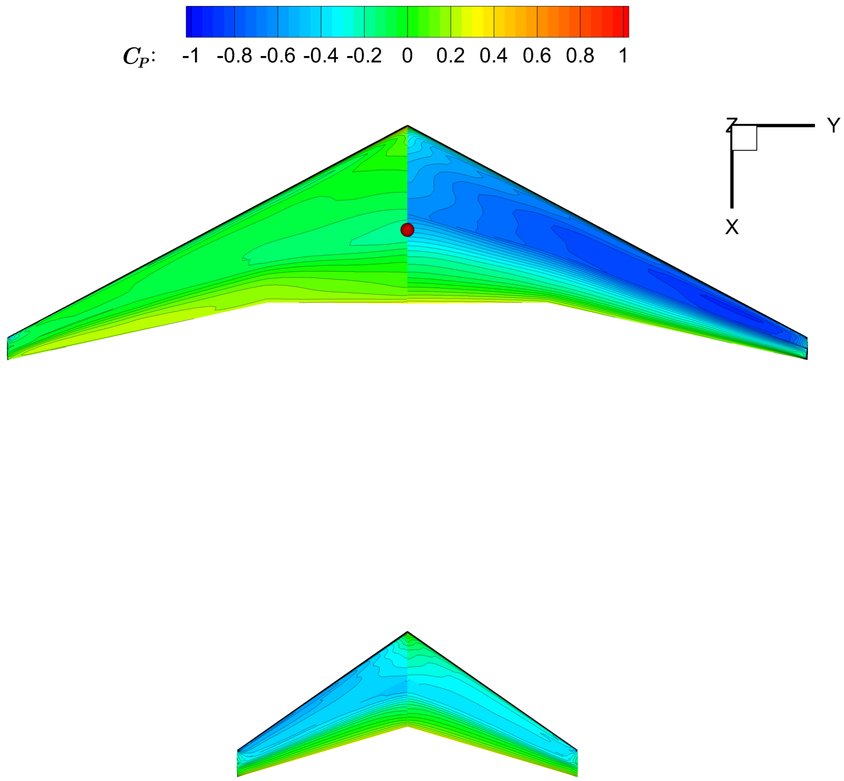

Figure 8: CTW100: Surface pressure coefficient contours over the lower (left) and upper (right) surfaces of the optimized wing-tail geometry. The red sphere represents the CG.

down pitching moment. On the other hand, Figure 9(b) shows that the spanwise lift distribution over the horizontal stabilizer is much closer to elliptical, but negative. This implies that a downforce from the horizontal stabilizer is necessary to maintain steady level flight, and as a result, constitutes trim drag.

Figure 10 illustrates the initial and optimized pressure coefficient distributions and section shapes at six spanwise locations, namely, at the wing root, 20%, 40%, 60%, and 80% of the semispan, and the wing tip. Here, it can be seen that the optimizer has designed shock-free supercritical cambered airfoils, while introducing wash out, namely, a gradual decrease in incidence angle from the root to the tip. As demonstrated by Osusky et al.,[21] RANS-based aerodynamic shape optimization has led to pressure coefficient distributions that exhibit smooth pressure recoveries, favorable for maintaining attached boundary layers in viscous flow.

From the grid convergence study, the optimized wing-tail design was found to have a drag coefficient of $C_{D_\mathrm{W}} = 0.0164$ and a lift-to-drag ratio of $L/D_\mathrm{W} = 27.4$. When accounting for the drag contributions from the fuselage ($C_{D_\mathrm{F}} = 0.0100$) and the vertical stabilizer ($C_{D_\mathrm{V}} = 0.0010$), the drag coefficient of the optimized CTW100 is $C_D = 0.0274$, which corresponds to a lift-to-drag ratio of $L/D = 16.4$.

Although nearly identical in design, the conventional cantilever-wing regional aircraft of Reist and Zingg,[37] which models the fuselage, is characterized by a lift-to-drag ratio of 19.8. This difference can be attributed to the viscous drag of the carry-through regions included in the present study, which results in an overestimate of the total drag when accounting for the fuselage and vertical stabilizer drag approximations. Although this deficit might be mitigated by the more drag efficient lift produced by the carry-through regions of the wing when compared to the lift that a fuselage would otherwise provide, it is clear that a model of the fuselage should be included in a future work. Nonetheless, consistency is maintained between the aerodynamic shape optimizations of each aircraft. A summary of the optimization results is provided in Table 4.

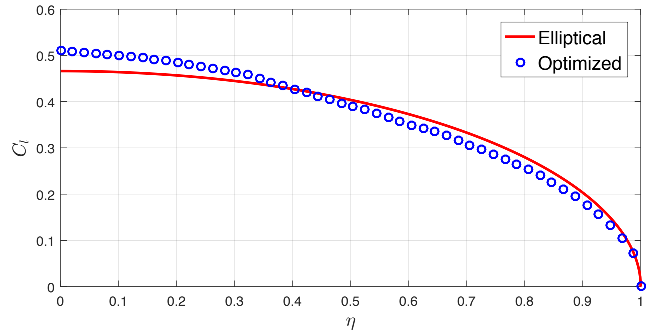

(a) Main wing

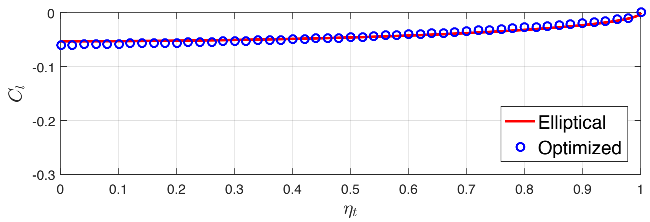

(b) Horizontal stabilizer

Figure 9: CTW100: Spanwise lift distribution.

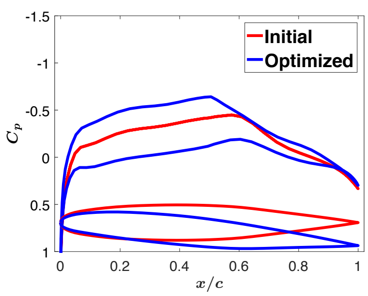

(a) Wing root

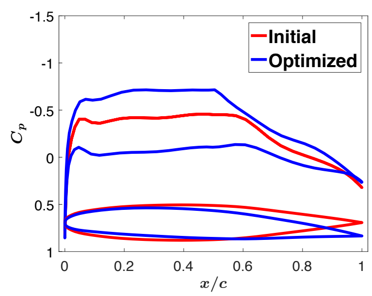

(b) 20% semispan

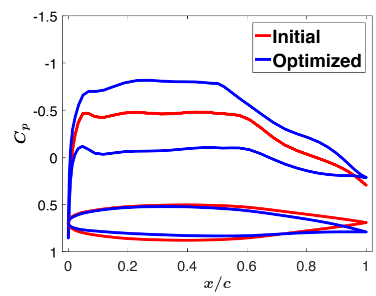

(c) 40% semispan

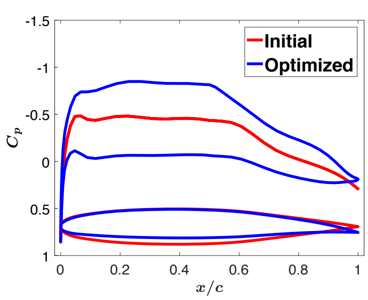

(d) 60% semispan

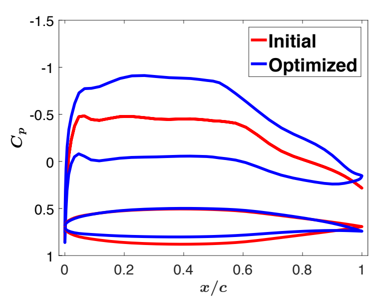

(e) 80% semispan

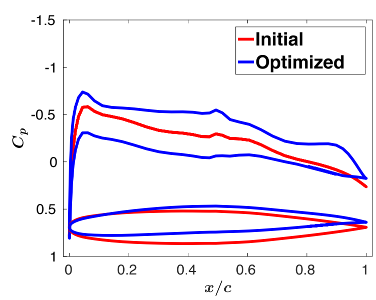

(f) Wing tip

Figure 10: CTW100: Pressure coefficient distributions and airfoil profiles.

Table 4: CTW100: Optimization results.

Weight [lb]	S [ft^2]	S_{wet} [ft^2]	C_L [–]	$C_{D_{\mathrm{W}}}$ [–]	L/D_{W} [–]	C_D [–]	L/D [–]	D/q_∞ [ft^2]	Drag [lb]
91,400	997	1,318	0.45	0.0164	27.4	0.0274	16.4	27.6	5,573

V. Exploratory Aerodynamic Shape Optimization

For the box-wing regional aircraft, aerodynamic shape optimization is performed following a two step process that includes exploratory optimization followed by lift-constrained drag minimization with somewhat reduced geometric freedom. For the first step, exploratory optimization is performed given significant geometric freedom and includes design variables such as leading-edge sweep, height-to-span ratio, and stagger-to-span ratio. Since these parameters can strongly influence structural weight, the objective of the optimization is to maximize the lift-to-drag ratio subject to a trim constraint, and bounds are set based on structurally-feasible box wing designs found from the literature.[9,11,17] In this way, aerodynamic trends and trade-offs related to leading-edge sweep, height-to-span ratio, stagger-to-span ratio, wing area, and wetted area can be investigated. The optimized design is then used as a basis for the initial geometry of the second step. For this step, lift-constrained drag minimization is performed where the optimization problem is to minimize drag subject to lift and trim constraints. In what follows, the exploratory optimization of the box wing is presented. This design is herein designated as the BWE.

A. Design Variables and Geometric Constraints

The exploratory optimization involves 809 design variables: the angle of attack, 35 twist degrees of freedom (one for each FFD-volume cross-section except at the root of the fore wing where it is replaced by the angle of attack design variable), 36 taper degrees of freedom (one for each FFD-volume cross-section), 720 section shape degrees of freedom (one for each FFD control point), 10 x-direction degrees of freedom (one for each axial curve control point from 2 to 11), 5 z-direction degrees of freedom (one for each axial curve control point from 7 to 11), and two CG degrees of freedom (the x- and z-coordinates). In conjunction with a number of linear geometric constraints, the x- and z-direction degrees of freedom are used to define more meaningful design variables such as leading-edge sweep, height-to-span ratio, and stagger-to-span ratio.

The leading-edge sweep design variables are realized through the x-direction degrees of freedom. For the fore wing, the leading-edge sweep is controlled by axial curve control point 3, with a linear equality geometric constraint imposed on axial curve control points 1, 2, and 3 that force them to remain collinear. Meanwhile, the leading-edge sweep of the aft wing is controlled by axial curve control points 10 and 11. In order to have the leading-edge sweep of the vertical tip fin vary in response to changes in the leading-edge sweep of the fore and aft wings, another linear equality geometric constraint, based on a linear interpolation, is imposed on axial curve control points 3 through 10, which also maintain the quality of the blended transitions. The leading-edge sweep design variables of the fore and aft wings are allowed to vary by ± 10 degrees in either direction, thus limiting their maximum bounds to wing sweep angles with reasonable structural weight.[9,11,17]

Meanwhile, the height-to-span ratio design variable is implemented through geometric constraints on the z-direction degrees of freedom. This is done through a series of linear equality geometric constraints on axial curve control points 7 through 11 that force them to move commensurately. In this work, the height-to-span ratio design variable is defined as an average based on the difference between the z-coordinates of axial curve control points 1 and 11 at the root of the fore and aft wings, respectively, and the difference between the z-coordinates of axial curve control points 3 and 10 at the tip of the fore and aft wings, respectively. The height-to-span ratio design variable is limited to ± 0.02 (i.e. height bounds of approximately 2 ft), which is chosen to keep the root chord of the aft wing close to the top of the vertical stabilizer, with structural considerations in mind.

Following a similar line of reasoning, the stagger-to-span ratio design variable is limited to ± 0.2 (i.e. stagger bounds of approximately ± 20 ft). This design variable is defined as the streamwise distance between axial curve control points 1 and 11, and is controlled by the x-direction degree of freedom of the latter. These bounds reflect the freedom that the wing system has to shift the root of the fore wing along the length

Table 5: BWE: Effective design variables and geometric constraints.

Parameter	Lower Bound	Upper Bound
Design Variables (798)		
Angle of attack (1)	$-8°$	$+8°$
Twist (35)	$-10°$	$+10°$
Taper (36)	50%	200%
Section shape (720)	50%	150%
Leading-edge sweep (2)	$-10°$	$+10°$
Height-to-span ratio (1)	-0.02	$+0.02$
Stagger-to-span ratio (1)	-0.2	$+0.2$
Streamwise CG (1)	$-\infty$	$+\infty$
Vertical CG (1)	$-\infty$	$+\infty$
Geometric Constraints (375)		
Wing volume (1)	$1.25V_{\text{fuel}}$	$+\infty$
Thickness-to-chord ratio (360)	80%	$+\infty$
Linear twist (6)	–	–
Linear taper (6)	–	–
Streamwise volume centroid (1)	x_V	x_V
Vertical volume centroid (1)	$0.12z_V + 0.88z_{\text{AC}}$	$0.12z_V + 0.88z_{\text{AC}}$

Bounds given as deviations and percentages are with respect to the initial geometry.

of the fuselage.

Through the height-to-span ratio and stagger-to-span ratio design variables, we intend to observe, if any, the trade-offs between geometric height and streamwise separation, and the wetted area of the vertical tip fin. In general, these represent trade-offs between induced drag and viscous drag; recall that for the box-wing configuration, an increase to the height-to-span ratio will lead to a decrease in induced drag. Similarly, an increase to the stagger-to-span ratio can reduce the mutual interference effects between the neighboring wings, which also reduces induced drag. However, in both instances, these benefits come with increased wetted area from the vertical tip fin, whose viscous drag will eventually overcome the advantage in induced drag. With these definitions, the number of effective design variables becomes 798.

As with the CTW100, minimum wing volume, minimum thickness-to-chord ratio, and linear twist constraints are imposed. In addition, a linear taper constraint, similar in definition to the linear twist constraint, is applied across each FFD volume. Together with any linear leading-edge constraints (i.e. the collinearity constraint on the axial curve control points of the fore wing), the linear taper constraint prevents the optimizer from designing nonlinear planforms through trailing-edge variations. This is done for reasons of manufacturability and to keep the design at current technology levels (e.g. for compatibility with conventional flap systems). Although a minimum planform area constraint may also be necessary for ensuring that a sufficient amount of lift can be generated at takeoff, we anticipate that the planform area will be effectively limited by the minimum taper bounds, the minimum wing volume constraint, and the minimum thickness-to-chord ratio constraints, thus preventing the wing from becoming undersized.

Lastly, the x- and z-coordinates of the CG are constrained based on the volume centroid of the wing system as described in Section III. In this way, the effect of the CG (and therefore the effect of the distribution of the total volume over the fore wing, the aft wing, and the vertical tip fin) on aerodynamic performance is made transparent to the optimizer. This opens the possibility for trades between volume distribution and any competing parameter. Table 5 summarizes the effective design variables and geometric constraints for the exploratory aerodynamic shape optimization of the BWE.

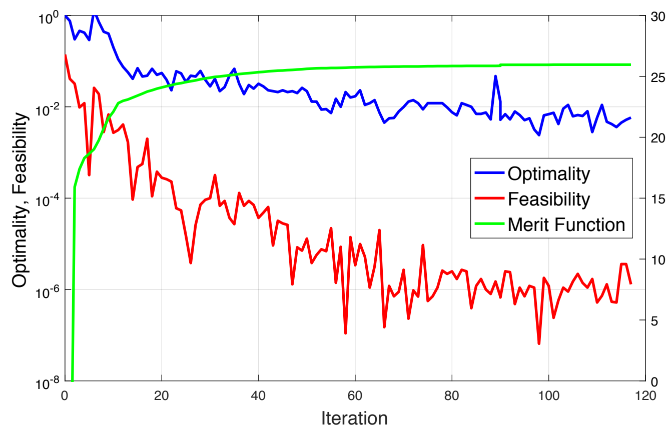

Figure 11: BWE: Optimization history. The Merit function represents L/D_{W}.

B. Lift-to-Drag Ratio Maximization

The optimization problem is formulated as follows:

$$\begin{aligned} \text{maximize} \quad & L/D_{\mathrm{W}}, \\ \text{w.r.t.} \quad & \mathbf{v}, \\ \text{s.t.} \quad & C_M = 0, \\ & \mathcal{C}_{\mathrm{geo}} = 0, \quad \mathcal{G}_{\mathrm{geo}} \geq 0, \end{aligned}$$

where L/D_{W} is the lift-to-drag ratio of the wing system, $\mathbf{v} = [\alpha, x_{\mathrm{CG}}, z_{\mathrm{CG}}, \mathbf{v}_{\mathrm{geo}}^{\mathrm{T}}]^{\mathrm{T}}$ is the vector of design variables, and $\mathcal{C}_{\mathrm{geo}}$ and $\mathcal{G}_{\mathrm{geo}}$ are the vectors of geometric equality and inequality constraints, respectively. As provided in Table 5, $\mathcal{C}_{\mathrm{geo}}$ consists of the linear twist, linear taper, streamwise volume centroid, and vertical volume centroid constraints, while $\mathcal{G}_{\mathrm{geo}}$ includes the minimum wing volume and minimum thickness-to-chord ratio constraints. A nominal cruise mission is considered at a Mach number of 0.78 and an altitude of 36,000 ft, which corresponds to a Reynolds number of 19.78×10^6, based on an MAC of 11.03 ft.

An optimized design was obtained following the completion of 117 design iterations on 288 processors. As shown in Figure 11, Feasibility converged to an approximate tolerance of 10^{-6}, Optimality has reduced by two orders of magnitude, and the Merit function has converged to a value of $L/D_{\mathrm{W}} = 26.0$ on the optimization grid. From the grid convergence study, the lift-to-drag ratio of the box wing was found to be $L/D_{\mathrm{W}} = 32.0$, which corresponds to a lift and drag coefficient of $C_L = 0.48$ and $C_{D_{\mathrm{W}}} = 0.0150$, respectively.

The optimized BWE has a height-to-span ratio of 0.25 and a stagger-to-span ratio of 0.78. The former reached its upper bound while the latter settled on an intermediate value. The sweep design variables of the fore and aft wings reached their upper and lower bounds, respectively, namely, +10 degrees for the fore wing and −10 degrees for the aft wing. The trim constraint led to a design with an evenly distributed planform area between the fore and aft wings; the relative planform area was found to be $S_{\mathrm{f}}/(S_{\mathrm{f}}+S_{\mathrm{a}}) = 0.46$. Furthermore, the chord lengths at axial curve control points 1, 2, 3, 10, and 11 did not reach their upper or lower bounds, but instead settled on an intermediate value. However, the chord lengths at axial curve control points 6 and 7 reduced to their minimum. This suggests that the vertical tip fin is seen as either unnecessary by the optimizer or that only a modest butterfly-shaped side-force distribution is required to complete the closed-loop circulation pattern. Nonetheless, the optimizer achieved a minimum volume design. The optimized geometry has a wing area of 1,229 ft^2 and a wetted area of 1,320 ft^2, namely, a 26% and a 27% reduction from the initial geometry, respectively. The optimized BWE is designed for an angle of attack of −0.17 degrees.

Figure 12(a) illustrates the pressure coefficient contours over the upper surface of the initial and optimized designs, while Figures 12(b) and 12(c) show the inboard and outboard surface pressure coefficient contours of the optimized design, respectively. From these, it can be seen that the suction side of the surface pressure coefficient distribution continues from the upper surface of the fore wing up the inboard surface of the vertical tip fin until the midspan, at which point the suction side continues up the outboard surface of the vertical

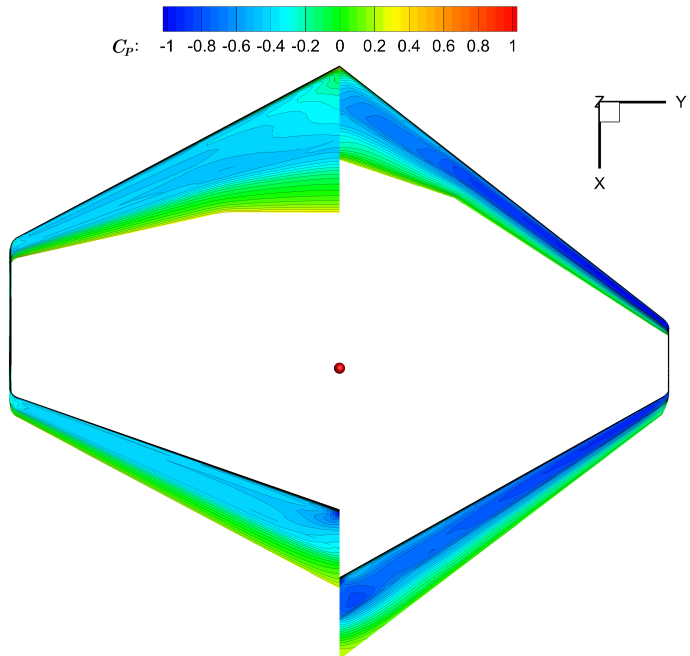

(a) Top view

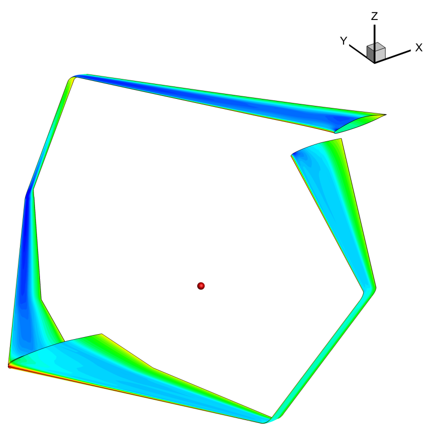

(b) Inboard view

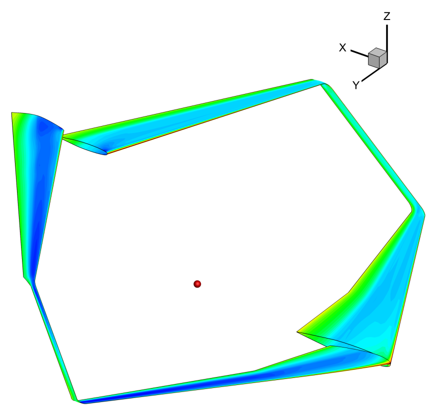

(c) Outboard view

Figure 12: BWE: Surface pressure coefficient contours for the initial [left, (a)] and optimized [right, (a)] wing geometries. Inboard and outboard views illustrate the signature closed-loop circulation pattern of the box wing. The CG of the optimized design is represented by the red sphere.

tip fin, and proceeds along the upper surface of the aft wing. This forms the closed-loop circulation pattern shown in Figure 13, which resembles the pattern predicted by linear aerodynamic theory. Given that the sectional force coefficient over the vertical tip fin remains small near the ends, it can be argued that the box wing only requires a small vertical tip fin to complete the closed-loop circulation.

The CG is represented by the red sphere in Figure 12, which is located 43.20 ft and 2.79 ft from the leading edge of the fore wing root along the x- and z-axes, respectively. Here, we can see that the CG has a slight bias towards the aft wing, as indicated by the relative planform area, but also due to a minor difference in wing volume. With regard to the latter, the section shapes near the root of the aft wing are relatively thick to account for the negative induced flow curvature caused by the fore wing, as noted by Wolkovitch.[10]

Having observed the expected aerodynamic characteristics of the box-wing aircraft configuration, the optimized design obtained here is used as a basis for the initial geometry of the following lift-constrained

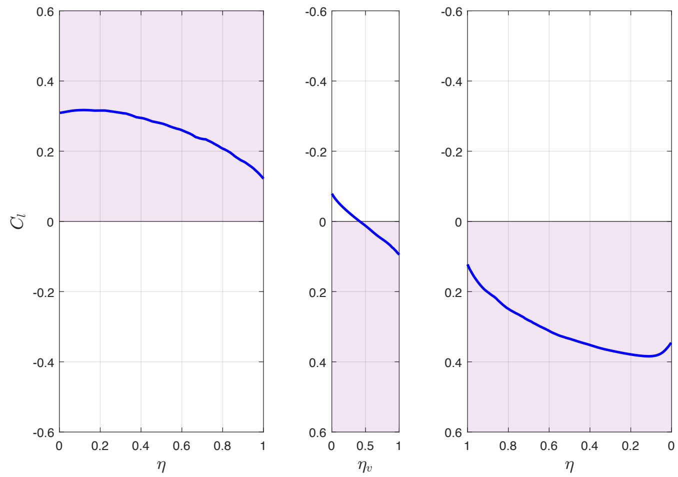

Figure 13: BWE: Force distributions over the fore wing (left), the vertical tip fin (middle), and the aft wing (right).

drag minimization. Design variables such as leading-edge sweep, height-to-span ratio, and stagger-to-span ratio will no longer be included since their maximum bounds, which were based on structural considerations, have been exhausted. For similar reasons, the taper design variable will be held fixed for the vertical tip fin. With regard to the fore and aft wings, however, taper design variables will still be included, albeit with less freedom to allow the design to be adjusted for the lift constraint.

VI. Lift-Constrained Drag Minimization of the Box Wing

Aerodynamic shape optimization based on the RANS equations is now applied to the aerodynamic design of a box-wing regional aircraft, herein designated as the BW100, in order to evaluate its potential for reduced fuel burn relative to the optimized CTW100. The initial planform, based on the optimized BWE, is depicted in Figure 14 alongside the updated free-form and axial deformation geometry control system and surface mesh.

A. Design Variables and Geometric Constraints

For the BW100, planform design variables such as leading-edge sweep, height-to-span ratio, stagger-to-span ratio are held fixed. However, taper design variables are still active for the fore and aft wings, and are permitted to vary by $\pm 10\%$ at a given FFD-volume cross-section. This is done to allow the optimizer the freedom to adjust the relative planform area for a lift target that is lower than that of the BWE optimization; recall that for the BWE optimization, the objective was to maximize the lift-to-drag ratio, leading to a relatively high lift coefficient. In total, there are 784 design variables: the angle of attack, 35 twist degrees of freedom (one for each FFD-volume cross-section except at the root of the fore wing), 26 taper degrees of freedom (one for each FFD-volume cross-section on the fore wing, the aft wing, and the two blended transitions), 720 section shape degrees of freedom (one for each FFD control point), and two CG degrees of freedom (the x- and z-coordinates).

Geometric constraints include minimum wing volume, minimum thickness-to-chord ratio, linear twist, and linear taper. As with the exploratory optimization, the CG is also constrained based on the volume centroid of the wing system. A summary of the design variables and geometric constraints is provided in Table 6.

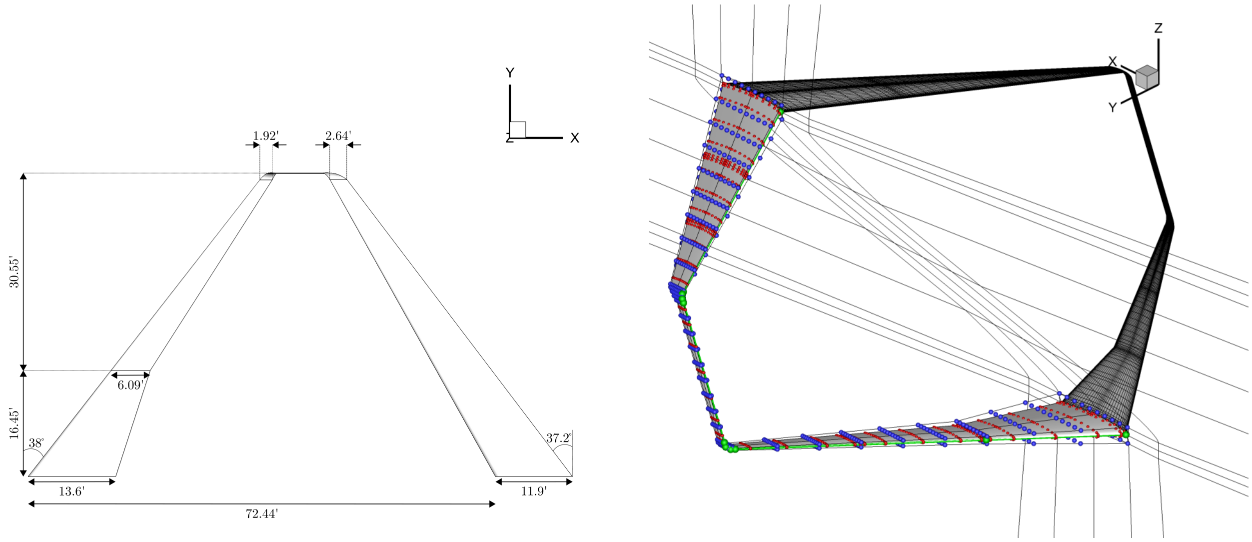

(a) Initial planform

(b) Geometry control system and surface mesh

Figure 14: BW100: Problem setup.

Table 6: BW100: Design variables and geometric constraints.

Parameter	Lower Bound	Upper Bound
	Design Variables (784)	
Angle of attack (1)	$-8°$	$+8°$
Twist (35)	$-10°$	$+10°$
Taper (26)	90%	110%
Section shape (720)	50%	150%
Streamwise CG (1)	$-\infty$	$+\infty$
Vertical CG (1)	$-\infty$	$+\infty$
	Geometric Constraints (374)	
Wing volume (1)	$1.25V_{\text{fuel}}$	$+\infty$
Thickness-to-chord ratio (360)	80%	$+\infty$
Linear twist (6)	–	–
Linear taper (5)	–	–
Streamwise volume centroid (1)	x_V	x_V
Vertical volume centroid (1)	$0.12z_V+0.88z_{\text{AC}}$	$0.12z_V+0.88z_{\text{AC}}$

Bounds given as deviations and percentages are with respect to the initial geometry.

Table 7: BW100: Design summary.

PAX	b [ft]	S [ft^2]	AR [–]	MAC [ft]	OEW [lb]	MTOW [lb]	Weight* [lb]
100+5	94	1,203	7.34	8.05	59,200	105,500	91,400

*The weight of the aircraft at the start of the nominal cruise mission.

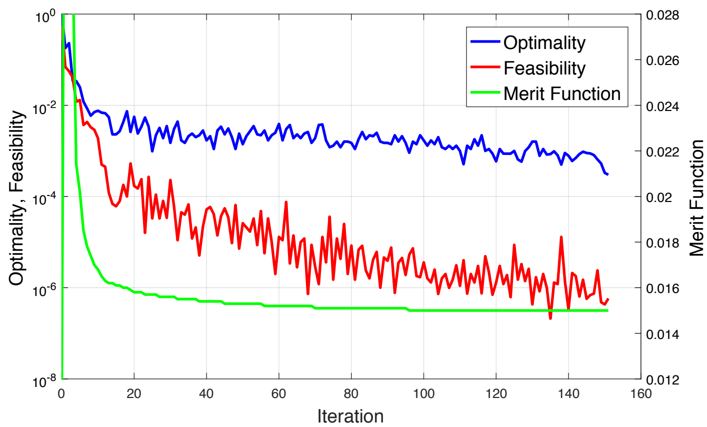

Figure 15: BW100: Optimization history. The Merit function represents C_{D_W}.

B. Lift-Constrained Drag Minimization

The optimization problem is formulated as:

$$\begin{aligned} \text{minimize} \quad & C_{D_\mathrm{W}}, \\ \text{w.r.t.} \quad & \mathbf{v}, \\ \text{s.t.} \quad & L = W, \quad C_M = 0, \\ & \mathcal{C}_\mathrm{geo} = 0, \quad \mathcal{G}_\mathrm{geo} \geq 0, \end{aligned}$$

where C_{D_W} is the drag coefficient of the wing system, $\mathbf{v} = [\alpha, x_\mathrm{CG}, z_\mathrm{CG}, \mathbf{v}_\mathrm{geo}^\mathrm{T}]^\mathrm{T}$ is the vector of design variables, and $\mathcal{C}_\mathrm{geo}$ and $\mathcal{G}_\mathrm{geo}$ are the vectors of geometric equality and inequality constraints, respectively. As provided in Table 6, $\mathcal{C}_\mathrm{geo}$ consists of the linear twist, linear taper, streamwise volume centroid, and vertical volume centroid constraints, while $\mathcal{G}_\mathrm{geo}$ includes the minimum wing volume and minimum thickness-to-chord ratio constraints. A nominal cruise mission is considered at a Mach number of 0.78 and an altitude of 36,000 ft, which corresponds to a Reynolds number of 14.5×10^6 based on an MAC of 8.05 ft. The maximum weight at cruise is equal to that of the CTW100, i.e. 91,400 lb, as discussed in Section III. A summary of the BW100 design is provided in Table 7

In total, 151 design iterations were completed on 288 processors. From Figure 15, it can be seen that Feasibility has been satisfied to an absolute tolerance of 10^{-6} and Optimality has been reduced by two orders of magnitude. With Feasibility met, the Merit function represents the drag coefficient, which converged to a value of $C_{D_\mathrm{W}} = 0.0154$ on the optimization grid.

The optimized BW100 is characterized by an angle of attack of 0.35 degrees and is a minimum volume design with a wing area of 1,203 ft^2 and a wetted area of 1,290 ft^2. Compared to the main wing of the CTW100, the optimized BW100 has 21% more wing area, thus satisfying takeoff requirements. Meanwhile, the optimized BW100 has 2% less wetted area than the total wetted area of the CTW100. Geometrically, this was made possible by the significantly lower wing volume of the BW100. The relative planform area between the fore and aft wings is $S_\mathrm{f}/(S_\mathrm{f} + S_\mathrm{a}) = 0.44$. For reference, the height-to-span and stagger-to-span ratio, which were not permitted to vary, have values of $h/b = 0.25$ and $l/b = 0.77$, respectively. The CG is

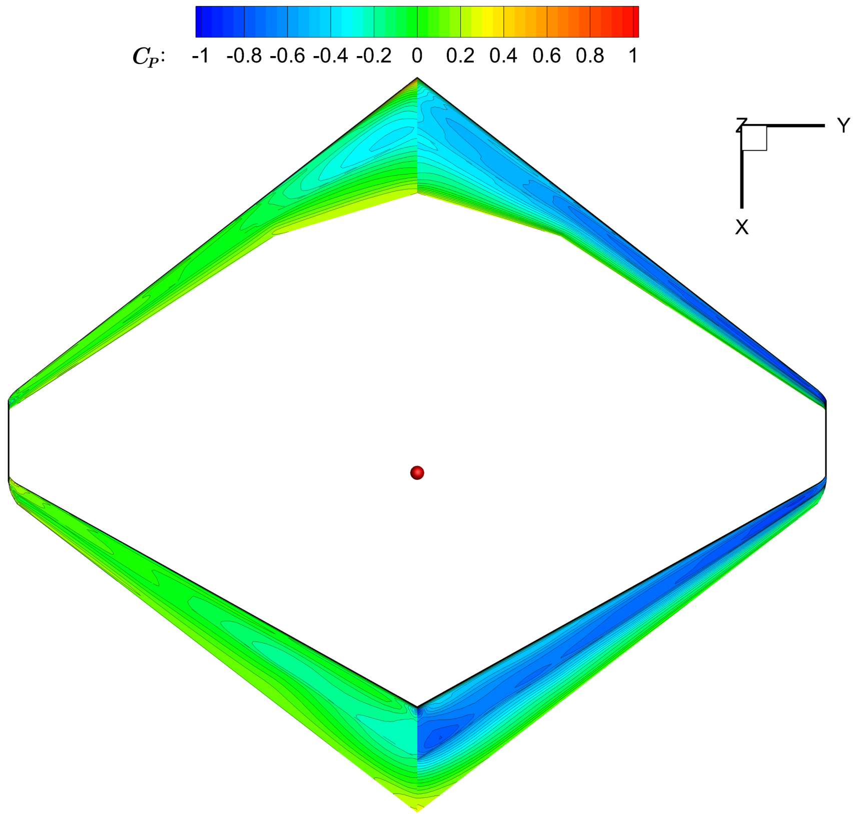

Figure 16: BW100: Surface pressure coefficient contours over the lower (left) and upper (right) surfaces of the optimized wing geometry. The red sphere represents the CG.

located 45.55 ft and 2.94 ft from the leading edge of the fore wing root along the x- and z-axes, respectively.

Figure 16 illustrates the pressure coefficient contours over the lower and upper surfaces of the optimized BW100. As with the optimized CTW100, the variations in the surface pressure contours are smooth, hinting at the shock-free nature of the design. Figures 17, 18, and 19 show the pressure coefficient distributions and section shapes of the initial and optimized designs at various spanwise and height locations for the fore and aft wings, and the vertical tip fin, respectively. These are taken at the wing root (bottom), 20%, 40%, 60%, and 80% of the semispan (height), and the wing tip (top) of the fore and aft wings (vertical tip fin). Here, it can be seen that the optimizer has designed supercritical cambered airfoils that are well-suited for transonic flow conditions. The pressure coefficient distributions show that the airfoil designs are indeed shock-free and exhibit gradual pressure recoveries.

The airfoil sections are also distinct at a number of spanwise stations on the fore and aft wings, which result from their adaptation to the induced flow curvature. Most apparent are the root sections of the fore and aft wings, which appear to be influenced by induced camber and angle of attack.[7,10,42] A close inspection of the surface pressure contours suggests that the downward bulge at the midchord of the fore wing and the upward bulge at the midchord of the aft wing have the purpose of preventing flow separation, unique to the flow interaction between each lifting surface. The protrusion at the root of the aft wing may also be the result of cross-flow from the forward-swept wing.

As found by Gagnon and Zingg,[18] the fore and aft wings are characterized by wash out (where the incidence angle decreases from the root to the tip) and wash in (where the incidence angle increases from the root to the tip), respectively. Furthermore, the force vector changes gradually from inboard to outboard from the bottom to the top of the vertical tip fin. Collectively, this forms the signature closed-loop circulation pattern shown in Figure 20.

A plane cut of the normalized z-component of momentum is plotted one MAC length downstream of the optimized BW100 in Figure 21. Here, it is clear that the optimized box-wing configuration produces an

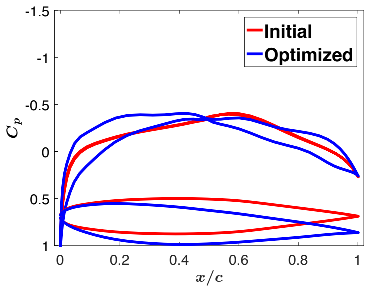

(a) Wing root

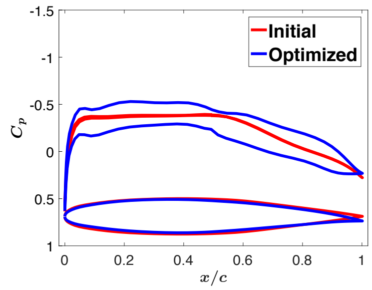

(b) 20% semispan

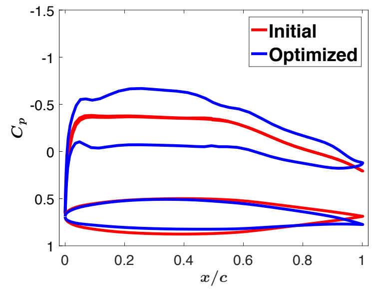

(c) 40% semispan

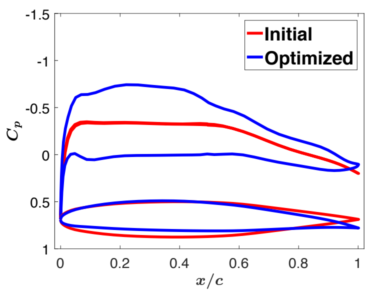

(d) 60% semispan

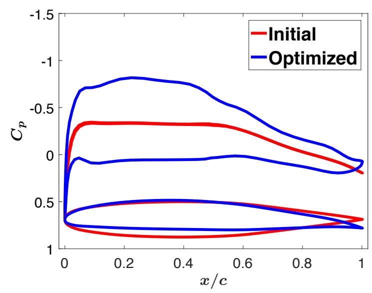

(e) 80% semispan

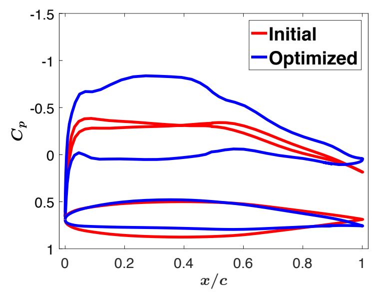

(f) Wing tip

Figure 17: BW100: Pressure coefficient distributions and airfoil profiles for the fore wing of the box-wing aircraft configuration.

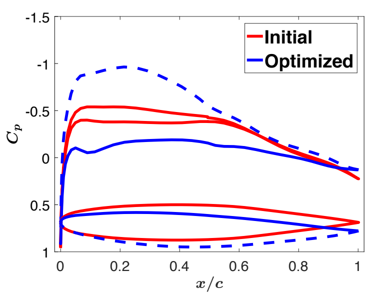

(a) Bottom

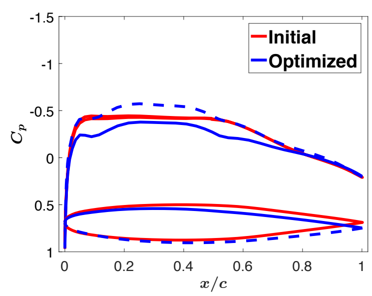

(b) 20% height

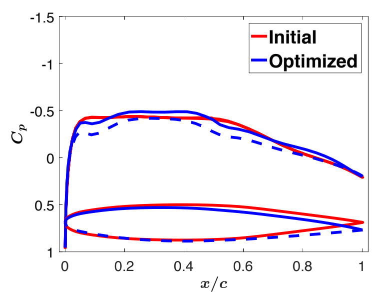

(c) 40% height

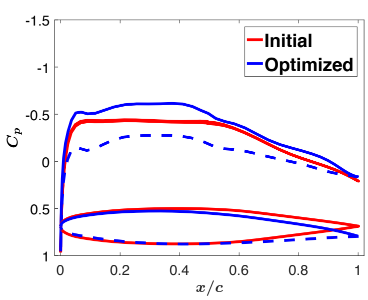

(d) 60% height

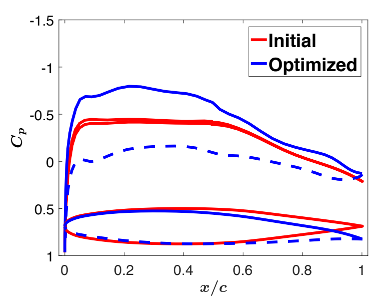

(e) 80% height

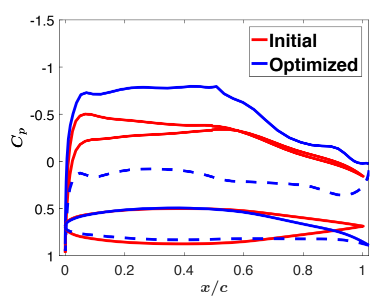

(f) Top

Figure 18: BW100: Pressure coefficient distributions and airfoil profiles for the vertical tip fin of the box-wing aircraft configuration. For the optimized geometry, solid lines represent outboard surfaces, and dashed lines represent inboard surfaces.

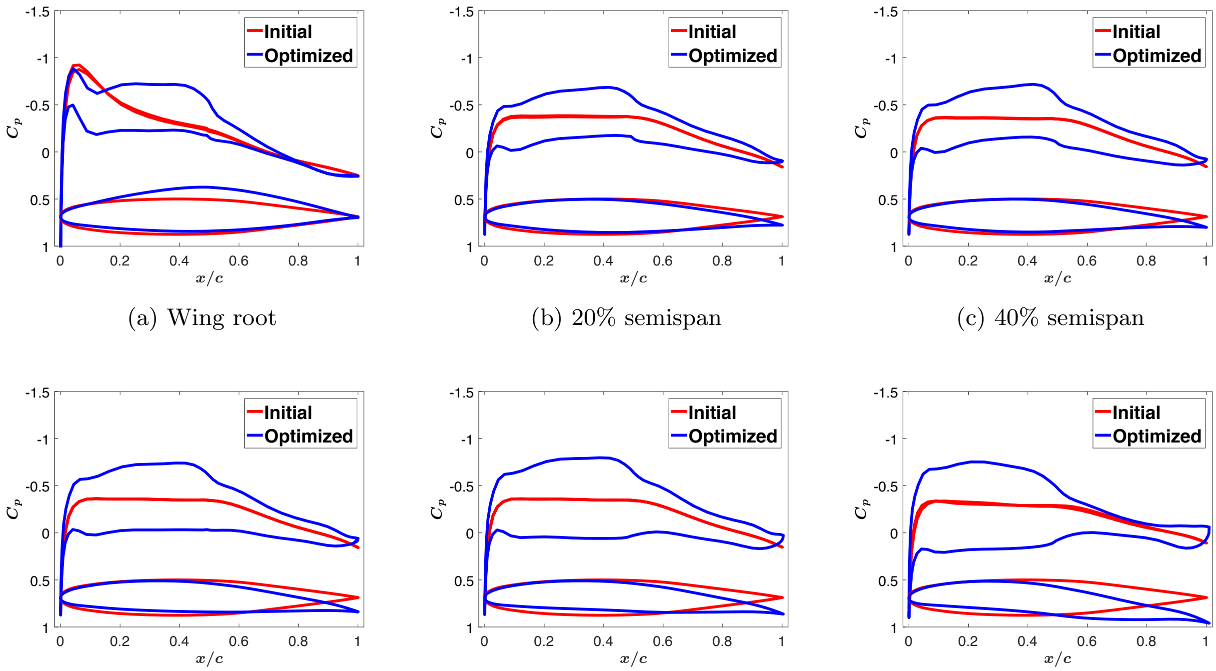

(a) Wing root (b) 20% semispan (c) 40% semispan

(d) 60% semispan (e) 80% semispan (f) Wing tip

Figure 19: BW100: Pressure coefficient distributions and airfoil profiles for the aft wing of the box-wing aircraft configuration.

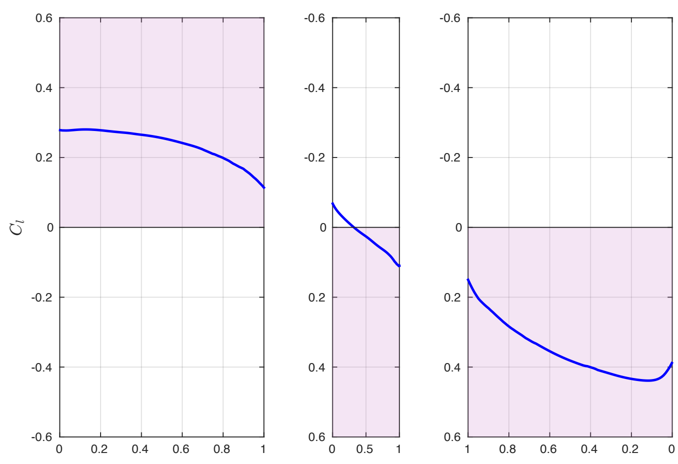

Figure 20: BW100: Force distributions over the fore wing (left), the vertical tip fin (middle), and the aft wing (right).

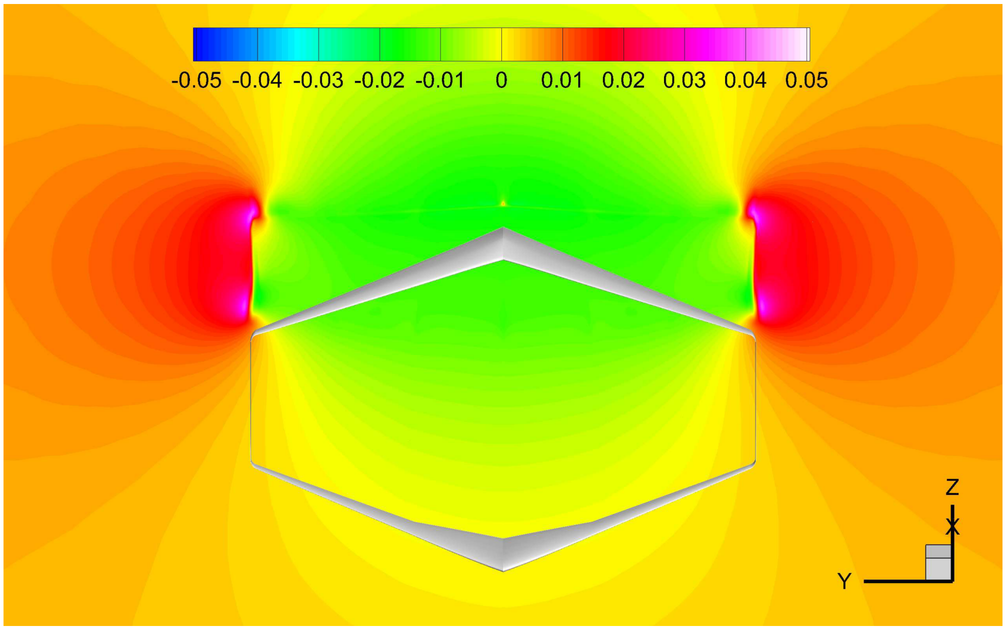

Figure 21: BW100: Plane cut of the normalized z-component of momentum located one MAC length downstream of the optimized wing geometry.

Table 8: BW100: Optimization results.

Weight [lb]	S [ft^2]	S_{wet} [ft^2]	C_L [–]	$C_{D_{\mathrm{W}}}$ [–]	L/D_{W} [–]	C_D [–]	L/D [–]	D/q_∞ [ft^2]	Drag [lb]
91,400	1,203	1,290	0.37	0.0116	31.9	0.0207	17.9	25.4	5,135

organized trailing-wake vortex structure that maximizes the separation between the high and low pressure regions below and above the wing system, respectively, thus lowering the vertical components of momentum. Such a feature is indicative of a minimum induced drag design.

From the grid convergence study, the drag coefficient of the wing design was found to be $C_{D_{\mathrm{W}}} = 0.0116$, which corresponds to a lift-to-drag ratio of $L/D_{\mathrm{W}} = 31.9$. When accounting for the viscous drag contributions from the fuselage ($C_{D_{\mathrm{F}}} = 0.0083$) and the vertical stabilizer ($C_{D_{\mathrm{V}}} = 0.0008$), the drag coefficient is $C_D = 0.0207$. This translate to a lift-to-drag ratio of $L/D = 17.9$. Based on Equation (2), the optimized BW100 thus burns 7.2% less fuel than the optimized CTW100 at cruise. A summary of the optimization results can be found in Table 8.

VII. Weight Sensitivity

One of the assumptions made during the performance study of the box-wing configuration was that of equal MTOW between the BW100 and CTW100 aircraft. This assumption was necessitated by the inapplicability of the empirical weight models to unconventional aircraft configurations such as the box wing. The incorrect use of such methods would make less clear whether the improvement in performance offered by the BW100 over the CTW100 was attributed to the aerodynamic advantages of the former or to the limitations of the approximation.

This decision was also supported by the work of Andrews and Perez[17] and Canto et al.[11] who demonstrated that the wing weight to MTOW ratio of a box wing is similar to that of an equivalent conventional baseline. In particular, Andrews and Perez applied a structural weight model to a box-wing aircraft configuration sized for short-range transport, and determined that the wing weight of the box wing was 5.7%

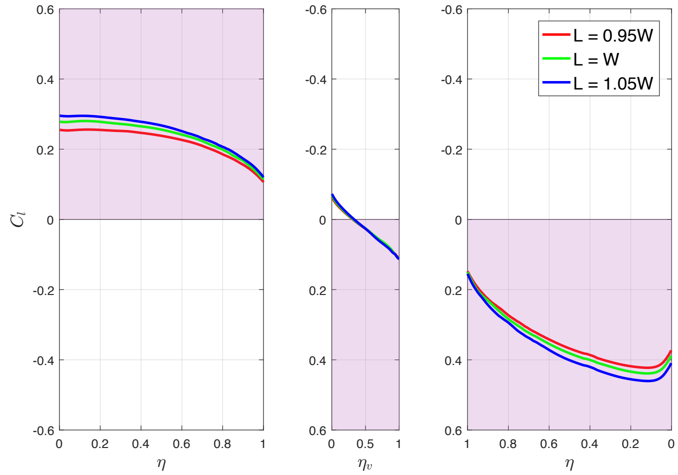

Figure 22: Weight Sensitivity: Force distributions over the fore wing (left), the vertical tip fin (middle), and the aft wing (right).

Table 9: Weight Sensitivity: Optimization results.

Design	Weight [lb]	S [ft^2]	S_{wet} [ft^2]	C_L [–]	C_D [–]	L/D [–]	D/q_∞ [ft^2]	Drag [lb]	Δ_{fuel} [%]
CTW100	91,400	997	1,318	0.45	0.0274	16.4	27.6	5,573	–
BW100-5	86,830	1,202	1,290	0.35	0.0203	17.2	25.0	5,048	-9.1
BW100	91,400	1,203	1,290	0.37	0.0207	17.9	25.2	5,106	-7.2
BW100+5	95,970	1,208	1,295	0.39	0.0212	18.4	25.8	5,216	-4.8

Δ_{fuel} is the cruise fuel-burn relative to the optimized CTW100.

less than that of a similar cantilever wing; this translated to a box wing with 2.2% less MTOW than the cantilever wing. From the work of Canto et al., it was found that a box-wing configuration of aluminum construction, when accounting for the twin vertical stabilizers, has a wing weight to MTOW ratio ranging from 15.8% to 17.5%, depending on the size and mission of the aircraft, which places it within range of the values exhibited by conventional designs.

Nonetheless, a weight sensitivity analysis can be useful to provide insight as to how the assumption of equal weight can affect the overall predicted performance of the box-wing aircraft configuration. More specifically, it can aid in understanding the effect that changes in weight have on aerodynamic performance, which can be due to the greater structural efficiency offered by the braced wing system, or the greater structural support required by a twin vertical stabilizer design. To this end, the lift-constrained drag minimization is repeated twice: once with a 5% increase to the maximum weight at cruise, and once with a 5% decrease to the maximum weight at cruise.

Figure 22 illustrates the closed-loop circulations produced for each lift target. Here it can be seen that the fore and aft wings adjust the amount of lift in a way that is proportional to the change in target lift. Furthermore, little to no change is observed from the side-force distribution over the vertical tip fin.

The results of the weight sensitivity study are summarized in Table 9 alongside the results of the CTW100 and the BW100 lift-constrained drag minimizations. If the weight of the BW100 were to increase by 5%, the fuel burn advantage over the CTW100 would decrease to 4.8%. On the other hand, if the weight of the box-wing regional aircraft were to decrease by 5%, the fuel burn advantage would increase to 9.1%. In both instances, the deviation in fuel-burn is modest, despite the sizeable change in maximum weight at cruise.

VIII. Conclusion

Aerodynamic shape optimization based on the RANS equations has enabled an in-depth study of a box-wing regional aircraft similar in size and mission to the Embraer E190. Exploratory aerodynamic shape optimization was performed with the objective of maximizing the lift-to-drag ratio subject to a trim constraint, given significant geometric freedom. Results indicate that the box wing benefits from a high aft-wing loading, which reduces the penalty paid in induced drag from the asymmetry in mutual induction, but because of the trim constraint, a more balanced planform design in which the loads carried by the fore and aft wings are closer to equilibrium is maintained. It was also found that the optimizer preferred to increase the height-to-span and stagger-to-span ratios in order to decrease induced drag, despite any increase to viscous drag arising from the higher wetted area of the vertical tip fin. Lastly, the optimized design was found to only require a modest butterfly-shaped side-force distribution on the vertical tip fin to complete the closed-loop circulation pattern. As a consequence, the optimized design featured a narrow vertical tip fin.

Having observed the aerodynamic trends and trade-offs predicted by linear aerodynamic theory, the design obtained from the exploratory optimization was used as a basis for the initial geometry of the ensuing lift-constrained drag minimization. The objective was to minimize drag with respect to twist, taper, and section shape degrees of freedom while subject to lift and trim constraints. Results indicate that the box-wing regional aircraft benefits from an 7.2% reduction in fuel burn relative to the optimized cantilever-wing design, over the course of a nominal cruise mission.

A weight sensitivity analysis was also performed in which the lift-constrained drag minimization was repeated for the box-wing aircraft configuration with a ±5% change in the lift target. From this study, it was found that a 5% decrease in cruise lift leads to an increase in fuel-burn advantage to 9.1% over the conventional baseline, whereas a 5% increase in cruise lift leads to a decrease in fuel-burn advantage to 4.8%. Given their conservative nature, these results suggest that a box-wing regional aircraft can provide a significant improvement in performance over a conventional cantilever-wing aircraft of the same class, despite uncertainties in structural weight.

Acknowledgments

Financial support is provided in part by the Natural Sciences and Engineering Research Council of Canada, the Ontario Graduate Scholarship, and the University of Toronto. Computations were performed on the General Purpose Cluster supercomputer at the SciNet HPC Consortium. SciNet is funded by: the Canada Foundation for Innovation under the auspices of Compute Canada; the Government of Ontario; the Ontario Research Fund - Research Excellence; and the University of Toronto.

References

[1]Kroo, I., "Nonplanar Wing Concepts for Increased Aircraft Efficiency," *Innovative Configurations and Advanced Concepts for Future Civil Transport Aircraft*, edited by E. Torenbeek and H. Deconinck, von Karman Institute for Fluid Dynamics, June 2005, VKI Lecture Series.

[2]Demasi, L., Monegato, G., Rizzo, E., Cavallaro, R., and Dipace, A., "Minimum Induced Drag Theorems for Joined Wings, Closed Systems, and Generic Biwings: Applications," *Journal of Optimization Theory and Applications*, Vol. 169, No. 1, 2016, pp. 236–261.

[3]Prandtl, L., "Induced Drag of Multiplanes," Tech. rep., NACA, March 1924, TN-182.

[4]Munk, M. M., "The Minimum Induced Drag of Aerofoils," Tech. rep., NACA, January 1921, TR-121.

[5]Demasi, L., Dipace, A., Monegato, G., and Cavallaro, R., "Invariant Formulation for the Minimum Induced Drag Conditions of Nonplanar Wing Systems," *AIAA Journal*, Vol. 52, No. 10, 2014, pp. 2223–2240.

[6]Frediani, A., "The Prandtl Wing," *Innovative Configurations and Advanced Concepts for Future Civil Transport Aircraft*, edited by E. Torenbeek and H. Deconinck, von Karman Institute for Fluid Dynamics, June 2005, VKI Lecture Series.

[7]Addoms, R. B. and Spaid, F. W., "Aerodynamic Design of High-Performance Biplane Wings," *Journal of Aircraft*, Vol. 12, No. 8, 1975, pp. 629–630.

[8]Miranda, L. R., "Boxplane Configuration - Conceptual Analysis and Initial Experimental Verification," Tech. rep., Lockheed-California Company, March 1972, LR-25180.

[9]Lange, R. H., Cahill, J. F., Bradley, E. S., Eudaily, R. R., Jenness, C. M., and MacWilkinson, D. G., "Feasibility Study of the Transonic Biplane Concept for Transport Aircraft Application," Tech. rep., The Lockheed-Georgia Company, June 1974, LG74ER0077.

[10]Wolkovitch, J., "The Joined Wing: An Overview," *Journal of Aircraft*, Vol. 23, No. 3, 1986, pp. 161–178.

[11]Canto, D. D., Frediani, A., Ghiringhelli, G. L., and Terraneo, M., "The Lifting System of a PrandtlPlane, Part 1: Design

and Analysis of a Light Alloy Structural Solution," *Variational Analysis and Aerospace Engineering: Mathematical Challenges for Aerospace design*, edited by G. Buttazzo and A. Frediani, Vol. 66, Springer US, Boston, MA, 2012, pp. 211–234.

[12]Divoux, N. and Frediani, A., "The Lifting System of a PrandtlPlane, Part 2: Preliminary Study on Flutter Characteristics," *Variational Analysis and Aerospace Engineering: Mathematical Challenges for Aerospace design*, edited by G. Buttazzo and A. Frediani, Vol. 66, Springer US, Boston, MA, 2012, pp. 235–267.

[13]Frediani, A., Cipolla, V., and Rizzo, E., "The PrandtlPlane Configuration: Overview on Possible Applications to Civil Aviation," *Variational Analysis and Aerospace Engineering: Mathematical Challenges for Aerospace design*, edited by G. Buttazzo and A. Frediani, Vol. 66, Springer US, Boston, MA, 2012, pp. 179–210.

[14]Oliviero, F. and Frediani, A., "Conceptual Design of a Very Large PrandtlPlane Freighter," *Variational Analysis and Aerospace Engineering: Mathematical Challenges for Aerospace design*, edited by G. Buttazzo and A. Frediani, Vol. 66, Springer US, Boston, MA, 2012, pp. 305–321.

[15]Frediani, A., Cipolla, V., and Oliviero, F., "Design of a Prototype of Light Amphibious PrandtlPlane," *56th AIAA/ASCE/AHS/ASC Structures, Structural Dynamics, and Materials Conference*, Kissimmee, Florida, January 2015, AIAA 2015-0700.

[16]Andrews, S. A. and Perez, R. E., "Parametric Study of Box-Wing Aerodynamics for Minimum Drag Under Stability and Maneuverability Constraints," *33rd AIAA Applied Aerodynamics Conference*, Dallas, Texas, June 2015, AIAA 2015-3291.

[17]Andrews, S. A. and Perez, R. E., "Multidisciplinary Analysis of a Box-Wing Aircraft Designed for a Regional-Jet Mission," *16th AIAA/ISSMO Multidisciplinary Analysis and Optimization Conference*, Dallas, Texas, June 2015, AIAA 2015-2793.

[18]Gagnon, H. and Zingg, D. W., "Aerodynamic Trade Study of a Box-Wing Aircraft Configuration," *Journal of Aircraft*, Vol. 53, No. 4, 2016, pp. 971–981.

[19]Gagnon, H. and Zingg, D. W., "Euler-Equation-Based Drag Minimization of Unconventional Aircraft," *Journal of Aircraft*, Vol. 53, No. 5, 2016, pp. 1361–1371.

[20]Elliott, J. K., *Aerodynamic Optimization based on the Euler and Navier-Stokes Equations using Unstructured Grids*, Ph.D. thesis, Massachusetts Institute of Technology, Cambridge, Massachusetts, USA, 1998.

[21]Osusky, L., Buckley, H. P., Reist, T. A., and Zingg, D. W., "Drag Minimization Based on the Navier-Stokes Equations Using a Newton-Krylov Approach," *AIAA Journal*, Vol. 53, No. 6, 2015, pp. 1555–1577.

[22]Cavallaro, R. and Demasi, L., "Challenges, Ideas, and Innovations of Joined-Wing Configurations: A Concept from the Past, an Opportunity for the Future," *Progress in Aerospace Sciences*, Vol. 87, No. 1, 2016, pp. 1–93.

[23]Hicken, J. E. and Zingg, D. W., "Aerodynamic Optimization Algorithm with Integrated Geometry Parameterization and Mesh Movement," *AIAA Journal*, Vol. 48, No. 2, 2010, pp. 400–413.

[24]Gagnon, H. and Zingg, D. W., "Two-Level Free-Form and Axial Deformation for Exploratory Aerodynamic Shape Optimization," *AIAA Journal*, Vol. 53, No. 7, 2015, pp. 2015–2026.

[25]Osusky, M. and Zingg, D. W., "Parallel Newton-Krylov-Schur Solver for the Navier-Stokes Equations Discretized Using Summation-By-Parts Operators," *AIAA Journal*, Vol. 51, No. 12, 2013, pp. 2833–2851.

[26]Pironneau, O., "On Optimum Design in Fluid Mechanics," *Journal of Fluid Mechanics*, Vol. 64, No. 1, 1974, pp. 97–110.

[27]Jameson, A., "Aerodynamic Design via Control Theory," *Journal of Scientific Computing*, Vol. 3, No. 3, 1998, pp. 223–260.

[28]Anderson, W. K. and Bonhaus, D. L., "Airfoil Design on Unstructured Grids for Turbulent Flows," *AIAA Journal*, Vol. 37, No. 2, 1999, pp. 185–191.

[29]Gill, P. E., Murray, W., and Saunders, M. A., "SNOPT: An SQP Algorithm for Large-Scale Constrained Optimization," *SIAM Journal on Optimization*, Vol. 14, No. 4, 2002, pp. 979–1006.

[30]Spalart, P. R. and Allmaras, S. R., "A One-Equation Turbulence Model for Aerodynamic Flows," *30th AIAA Aerospace Sciences Meeting and Exhibit*, Reno, Nevada, January 1992, AIAA 92-0439.

[31]Svärd, M., Mattsson, K., and Nordström, J., "Steady-State Computations Using Summation-by-Parts Operators," *Journal of Scientific Computing*, Vol. 24, No. 1, 2005, pp. 79–95.

[32]Del Rey Fernández, D. C., Hicken, J. E., and Zingg, D. W., "Review of Summation-by-Parts Operators with Simultaneous Approximation Terms for the Numerical Solution of Partial Differential Equations," *Computers & Fluids*, Vol. 95, No. 22, 2014, pp. 171–196.

[33]Jameson, A., Schmidt, W., and Turkel, E., "14th Fluid and Plasma Dynamics Conference," *Numerical Solution of the Euler Equations by Finite Volume Methods Using Runge-Kutta Time-Stepping Schemes*, Palo Alto, California, June 1981, AIAA-81-1259.

[34]Pulliam, T. H., "Efficient Solution Methods for the Navier-Stokes Equations," *Numerical Techniques for Viscous Flow Computation in Turbomachinery Bladings*, von Karman Institute for Fluid Dynamics, January 1986, VKI Lecture Series.

[35]Swanson, R. C. and Turkel, E., "On Central-Difference and Upwind Schemes," *Journal of Computational Physics*, Vol. 101, No. 2, 1992, pp. 292–306.

[36]Squire, W. and Trapp, G., "Using Complex Variables to Estimate Derivatives of Real Functions," *SIAM Review*, Vol. 40, No. 1, 1998, pp. 110–112.

[37]Reist, T. A. and Zingg, D. W., "High-Fidelity Aerodynamic Shape Optimization of a Lifting-Fuselage Concept for Regional Aircraft," *Journal of Aircraft*, 2016, (In press).

[38]Embraer Commercial Aircraft, *Embraer 190 Airport Planning Manual*, 2005, Revision 10 - 18 February 2013.

[39]Torenbeek, E., *Synthesis of Subsonic Airplane Design*, Delft University, 1st ed., 1976.

[40]Kroo, I., "Aircraft Design: Synthesis and Analysis," 2016.

[41]Raymer, D. P., *Aircraft Design: A Conceptual Approach*, American Institute of Aeronautics and Astronautics, 5th ed., 2012.

[42]Kuchemann, D., "Investigation of the Lift Distribution Over the Separate Wings of a Biplane," Tech. rep., NACA, October 1938, No. 889.